Snow/Firn Densification in Polar Ice Sheets

Andrey N. Salamatin [*, ****], Vladimir Ya. Lipenkov [**, ****], Jean Marc Barnola [***], Akira Hori [****], Paul Duval [***], Takeo Hondoh [****]

*Kazan State University, Kazan, Russia, Andrey.Salamatin@ksu.ru
**Arctic and Antarctic Research Institute, St. Petersburg, Russia
***Laboratoire de Glaciologie et Géophysique de l'Environnement, Grenoble, France
****Hokkaido University, Sapporo, Japan

Abstract: A sophisticated physical model of the dry snow/firn densification process in ice sheets is proposed. Macroscopically, snow and firn undergo vertical uniaxial compression with non-zero deviatoric stresses and strain rates. The present mathematical description of densification includes dilatancy and "force-chain" effects in snow and develops previous concepts of ice-particle rearrangement by grain-boundary sliding and sintering by power-law creep under overburden pressure. Both densification mechanisms work together during the first snow stage until the closest packing of ice grains is reached at critical densities of 0.7-0.76 and the firn stage controlled only by the dislocation creep sets on. In addition to the ice-grain coordination number and the slope of the radial distribution function, a new structural parameter is introduced to account for grain bonding (agglomeration) effects. The model is constrained and validated on direct stereological observations of ice core structures and a representative set of snow/firn density-depth profiles covering a wide range of present-day climatic conditions (−57.5 to −10 °C and ice accumulation at 2.15 to 330 cm yr^{-1}). Simple equations are derived for predicting the depth of pore closure in firn and the ice age at close-off. The paleoclimatic evolution of quasi-stationary density-depth profiles and close-off characteristics at Vostok Station (East Antarctica) are simulated and discussed.

Key words: ice sheet, snow/firn densification, physical model, paleoclimatic implication

List of symbols

a	Mean relative bond area in units of R^2
A	Mean relative area of the contact segment bases in units of R^2
A_c	Mean ice-grain area measured in thin sections
b	Accumulation rate in ice equivalent
B_h, B_t	Dimensionless form factors of the density-depth profile in Eqs. (25)
C	Relative slope of the cumulative ice-grain radial distribution function (RDF)
$\dot{\mathbf{E}}(\dot{E}_j)$	Strain rate tensor (principal strain rates, $j = 1, 2, 3$)
$\dot{e}_1$	Rate of ice thinning due to global ice-sheet motion
F	Rheological function in Eq. (7)
g	Gravity acceleration
G	Rheological function in Eq. (7)
h	Depth
k	Rate constant
p	Ice pressure produced by normal components of contact forces
p_l	Load pressure (hydrostatic overburden stress)
P	Macroscopic pressure in ice skeleton
Q	Activation energy
R ($\bar{R}$)	Mean equivalent-sphere current radius of ice grains (normalized by surface size R_s)
R', R''	Fictitious normalized radii of plastically deformed ice grains in the densification scheme [10]
R_g	Gas constant
s	Fraction of free ice-grain surface not involved in plastic contacts
s_b	Fraction of grain surface area involved in grain bonds
t	Time
T	Temperature (in K)
T_j	Principal macroscopic deviatoric stresses ($j = 1, 2, 3$)
w	Vertical velocity with respect to ice-sheet surface
x	Fraction of deviatoric deformations due to ice-grain rearrangement
Z	Coordination number
α	Power-creep exponent in Eq. (13)
β	Dilatancy exponent in Eq. (18)
γ	Lateral deviatoric strain rates
Γ	Coefficient in the grain boundary sliding model (12) in [2]
δ	Grain bond thickness
Δ	Ice-equivalent glacier thickness
ε	Correction coefficient in Eq. (15)
ζ	Fraction of free grain surface occupied by extra neck volume due to diffusive ice mass transfer (bonding factor)
η (η')	Kinematic (bulk) viscosity in Eq. (6)
λ	Dilatancy rate parameter in Eq. (3)
μ	Non-linear viscosity in power-creep law (13)
ν	Linear grain-boundary viscosity

ρ Relative density of snow/firn deposits
ρ_i Density of pure ice
Σ_j Principal macroscopic stresses (j = 1, 2, 3)
ω Densification (compression) rate

Superscripts
$'$ Fictitious geometric characteristics of ice grains in the densification scheme [10]
* Value at reference temperature T^* (Vostok Station)

Subscripts
c Ice crystal growth
off Close-off characteristic
p Ice-grain plasticity characteristic
r Ice-grain rearrangement characteristic
s Ice sheet surface
0 Critical point (snow-to-firn transition)

1. Introduction

Fresh snow deposited on a dry glacier surface is subjected within a few uppermost meters to various depositional, diagenetic, and meteorological processes [3]. Even in cold natural conditions, ice thermodynamically is relatively close to melting, being at high homologous temperature. There exist a variety of mass transfer mechanisms in the pressureless sintering of surface snow (e.g., [49]). Among them, evaporation-condensation (vapor transport) and surface diffusion play a primary role in the snow metamorphism [37, 58, 64] largely through the rounding and bonding of ice crystals [14, 35]. At depths of 2-3 m, snow is a low-density (porosity 50-65%) polydisperse compacted powder of ice grains. The properties of this structure are considered admittedly to originate from the surface snow characteristics which are ultimately climate controlled. Further on, particle rearrangement [6] and sintering under overburden pressure become the principal mechanisms of the snow/firn densification, leading to the formation of bubbly ice upon pore closure in deeper strata (50-150 m). Although studies [16, 22, 23, 49] show that plastic deformation (i.e., power-law dislocation creep) dominates in the development of intergranular contacts under loads exceeding 0.01-0.1 MPa, the pressureless sintering effects driven by the excess surface free energy of ice crystals still can not be ignored.

The transformation of snow into glacier ice, being a fundamental glaciological phenomenon, is also a key process that links paleoclimatic records of ice properties in glaciers to those of atmospheric gases trapped in the ice (e.g., [12, 15, 33, 65, 67]). The most important characteristics of the snow/firn densification process are the close-off depth and ice age as well as the grain size that ultimately determines the geometrical properties (size and number) of air inclusions (i.e., bubbles and hydrates) in polar ice sheets [45, 47]. Here we concentrate on snow/firn densification modeling as a primary step related to paleoreconstructions from ice core data. Predictions of the surface and close-off densities as well as ice-age/gas-age difference are considered as separate problems out of the scope of the present study.

The mechanical properties of snow and its densification at loading were originally studied and theoretically interpreted by Voytkovskiy [73]. Herron and Langway [39] subsequently proposed a density-depth (or age) relationship that is now widely employed as a phenomenological firnification model. However, the application of this relationship, as well as other semi-empirical approximations (e.g., [12, 19, 43, 71]) is of limited validity, being confined to the ranges of present-day environmental conditions covered by the experimental data. An alternative, although much more complicated approach is to develop a physical theory relating microstructural changes in the snow compact to its general macroscopic behavior during compression. In a series of papers [16, 17, 26, 38, 50], a suite of microstructural constitutive models were constructed, specifically for the case of snow under high loading rates (strain rates exceeding 10^{-5} s^{-1}). It was assumed that the deformation process and fracturing in the granular structure took place predominantly in relatively narrow necks connecting grain bodies. Such conditions differ substantially from those met in the natural snow/firn densification process at the glacier surface, where the strain rates are much lower, on the order of 10^{-11} to 10^{-9} s^{-1} and the intercrystalline contacts are well developed even at shallow depths [35]. The surface fraction of grain bonds is large [4, 7, 9], with neck-to-grain radii ratio of 0.6-0.7 [1, 2]. It is therefore conventionally accepted after Alley [2] that particle rearrangement, which dominates in the highly porous snow, is controlled by linear-viscous grain-boundary sliding. This microstructural physical description of the repacking mechanism can be directly incorporated into snow/firn densification models [8, 20].

The number of bonds per grain (i.e., coordination number) in snow increases with density, restricting intergranular sliding. As a result, the creep of ice grains in contact gradually prevails over, becoming the sole mechanism of firnification beyond a critical snow density and coordination number at which particle rearrangement essentially stops. This general scenario is commonly simplified by the assumption that the critical density separates two successive regimes of densification, either by grain boundary sliding (snow stage) or by plastic deformation (firn stage) (e.g., [8, 9]). Usually the transition between the two densification zones is identified after Anderson and Benson [6] with the specific bend found in the density-depth profile at a relative density of approximately 0.6. However, as suggested by Ebinuma and coworkers [23-25], this first critical point of sharp decrease in the densification rate may simply manifest the onset of an intermediate regime in which particle rearrangement and plasticity work together, while the dislocation creep takes over at higher relative densities of about 0.75.

A physical microstructural model for the firn stage of densification by power-law creep was constructed [9] based on a geometrical description of the dense random packing of monosize ice spheres [10, 29] and an approximate solution for the initial phase of plastic deformation of two contacting spheres [11, 76]. This model was linked to Alley's model [2] for ice-grain rearrangement in the snow stage (neglecting dislocation creep) by introducing the critical density as a variable (tuning) parameter. The principal problem encountered in such an approach was that the initial densely packed structure assumed in [10] had zero contact areas between particles at the critical density, whereas Alley's scheme described grain sliding over developed interfaces (i.e., grain boundaries). Hence, it was suggested [7-9] to represent firn densification by the plastic deformation of groups of ice crystals (aggregates, or agglomerates) rather than single grains. Clusters of ice crystals are distinguished in natural ice cores, and structures of ice-grain agglomerates can be considered as more realistic. However, in Arnaud's approach [8], the aggregates are defined without inner voids having the same specific surface area as the original ice skeleton at the snow-to-firn transition. Although this assumption avoids discontinuity in the parameterization of the ice-grain structure, crystal bonding and neck development are reduced to pure agglomeration, which, in a monosize approximation, is equivalent to simple rescaling of micro-dimensions of the ice-grain compact. Nevertheless, the model [8] allows the direct extension of computational simulations and theoretical predictions to various paleoclimatic and thermodynamic conditions (e.g., [15, 33]).

In the present study, aiming at a more complete and sophisticated representation of the microstructural picture of ice-grain kinematics and stress-strain distributions, we continue the elaboration of the snow/firn densification model recently started by Salamatin and coworkers [60]. The following aspects are of particular interest.

1. As there is no possibility for independent lateral (horizontal) constriction of snow deposits on an infinitely large ice sheet surface, natural densification of the snow, firn, and bubbly ice strata is, macroscopically, a process of uniaxial (vertical) compression with non-zero deviatoric stresses and strain rates superimposed on the global (deviatoric) deformation impacted by glacier motion [61]. This densification process can not be adequately modeled simply on the basis of hydrostatic compression as usually considered in powder metallurgy (e.g., [10, 76]).

2. Ice-grain rearrangement in snow under uniaxial compression in accordance with general concepts of granular media and soil mechanics (e.g., [18, 55, 56]) can not be geometrically arbitrary on the microscopic level and is thus subjected to certain kinematic constraints relating volumetric compression rates to effective deviatoric strain rates of particle restacking. This phenomenon is known as the dilatancy effect. For instance, the radial expansion of snow samples observed in axial compression tests [63] may, at least in part, be caused by the dilatant motion of ice grains as rigid particles.

3. Overburden pressure, increasing from the very beginning of snow densification, acts as intergranular contact forces that result equally in the rearrangement and plastic deformation of ice particles. In principle, these two firnification mechanisms operate simultaneously until restacking ceases at the critical coordination number (i.e., critical density). This suggests that Anderson and Benson's interpretation [6] of the bend around a relative density of 0.6 in the density-depth profiles should be re-examined.

4. Grain bonds in snow and firn are well developed [4, 9], and the mean bond radius in the snow stage remains largely constant [1, 2] despite the relative motion of grains. This suggests that water-vapor transport (pressureless sintering mechanisms), even if negligible as a densification factor, still acts in combination with grain creep in the neck-formation process and should thus be incorporated directly into any physical model of dry snow/firn densification. Such an improvement can not be achieved within the framework of [8], and additional reconciliation with Arzt's theory [10] is necessary.

5. According to [36], the granular ice skeleton carries the applied load in "force chains" and a certain fraction of grains in the polydisperse snow structure is essentially stress-free. This means that the effective pressure at the contacts of deforming ice spheres is much higher than in a uniformly loaded structure. Furthermore, as the mean grain coordination number, equal to ~7 at the critical density, increases by a factor of 2 in the firn stage [4, 7], the plastic deformation of ice in the vicinities of numerous contacts distributed over the grain surface is more similar to the creep of relatively thin contacting spherical segments than that for a single contact between two spheres (agglomerates) as assumed in [8, 9] after [10, 11]. Thus the plastic deformation of grains also requires a more accurate simulation.

With this in mind, we begin with the improved description of snow/firn densification, extending on [60]. The resultant physical model is evaluated and validated on available ice core texture measurements and a representative set of snow/firn density profiles covering the full range of present-day climatic conditions (temperature, accumulation rate, wind speed, and insolation). Finally, possible applications of the developed theory to analysis of the snow/firn densification process in changing climate are considered with special emphasis on predicting the close-off (depth and ice age) characteristics.

2. Theory of snow/firn densification

2.1. General notions and phenomenological equations

Let us consider the process of densification of snow/firn deposits under the load pressure (hydrostatic

overburden stress) p_l on a glacier surface in dry, cold climatic conditions. Due to lateral constraints, macroscopically it is a confined vertical (uniaxial) compression. We designate the corresponding component of the strain-rate tensor $\dot{\mathbf{E}}$ by subscript "1". The total deformations in the two other principal orthogonal (horizontal) directions "2" and "3" are equal to zero, and $\dot{\mathbf{E}}$ is determined as

$$\dot{E}_1 = -3\omega\ , \qquad \dot{E}_2 = \dot{E}_3 = 0\ ,$$
$$\omega = -\mathbf{tr}(\dot{\mathbf{E}})/3 = -(\dot{E}_1 + \dot{E}_2 + \dot{E}_3)/3\ .$$

The snow/firn densification (compression) rate ω coincides with the lateral deviatoric strain rate $\gamma = \dot{E}_2 - \mathbf{tr}(\dot{\mathbf{E}})/3 = \dot{E}_3 - \mathbf{tr}(\dot{\mathbf{E}})/3$, and, by definition,

$$\frac{1}{\rho}\frac{d\rho}{dt} = 3\omega\ , \qquad (1)$$

where ρ is the relative density (ice volume fraction) of the ice structure; t is the time, and d/dt is the particle derivative.

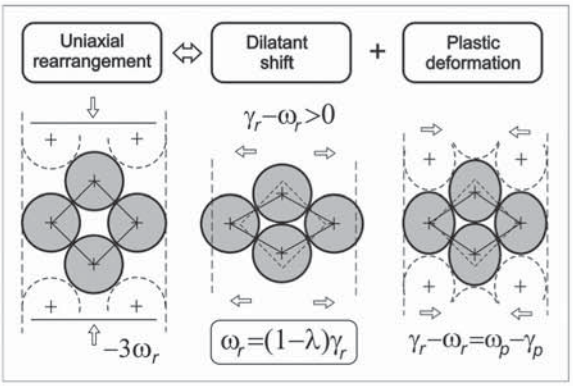

Figure 1: Interaction between dilatancy effects and plastic deviatoric deformations in snow densification by grain rearrangement. Only excess deviatoric creep compensating for lateral dilatant expansion is depicted in the last fragment.

The overall macroscopic deformation in the ice compact is the sum of two constituent parts due to (a) rearrangement (i.e., sliding) of grains as rigid particles and (b) grain plasticity by dislocation creep under contact forces. These two mechanisms are distinguished by the subscripts "r" and "p", respectively. Thus,

$$\omega = \omega_r + \omega_p = \gamma_r + \gamma_p = \gamma. \qquad (2)$$

These equations do not allow unique division between the restacking and plastic strain rates. The dilatancy [18, 55, 56] of the granular ice structure (see Fig. 1) should additionally be taken into account. This means that the uniaxial compression of ice powder, as an ensemble of rigid particles, can occur only at excess deviatoric strain, $\gamma_r > \omega_r$, and the total deformational compatibility in the ice compact presumes that the difference $\gamma_r - \omega_r$ is compensated for by extra plastic compression $\omega_p - \gamma_p$. Although the dilatancy in snow is generally small with respect to total deviatoric deformation, this effect controls the interaction between the two densification mechanisms. A conventional linear kinematic relation is assumed here between the densification rate due to grain rearrangement ω_r and the corresponding deviatoric deformation γ_r, i.e.,

$$\omega_r = (1 - \lambda)\gamma_r\ . \qquad (3)$$

Parameter λ determines the rate of dilatancy and, being a function of ρ, is one of the principal structural and deformational characteristics of snow as a granular material. It varies from 0 for ultimately friable, highly porous snow, when $\omega_r = \gamma_r$, to 1 in the critical (dense) packing state, when $\omega_r = 0$. Simultaneous equations (2) and (3) yield explicit expressions for the constituents of the strain rates via the total densification rate ω and the fraction x of the deviatoric deformations due to the ice crystal rearrangement:

$$\gamma_r = x\omega\ , \qquad \gamma_p = (1 - x)\omega\ ,$$
$$\omega_r = x(1 - \lambda)\omega\ , \qquad \omega_p = [1 - (1 - \lambda)\, x]\omega\ . \qquad (4)$$

The macroscopic stress tensor Σ_i is conventionally expressed via the isotropic pressure P and the vertical deviatoric stress T_1 ($T_2 = T_3 = -T_1/2$):

$$\Sigma_1 = -P + T_1\ , \qquad \Sigma_2 = \Sigma_3 = -P - T_1/2\ . \qquad (5)$$

Consequently, the problem of the snow/firn densification modeling is reduced to the construction of constitutive equations relating the deformation rates γ_r and γ_p (or ω_r and ω_p, or x and ω) to the averaged stresses P and T_1 in the granular ice material. In accordance with the general concepts, we write the rheological law for grain rearrangement by linear-viscous boundary sliding as

$$P = p + 3\eta'\omega_r\ , \qquad T_1 = -4\eta\gamma_r\ . \qquad (6)$$

Here η' and η are the coefficients of bulk and kinematic viscosity, and p is the pressure produced by the normal components of the contact forces (i.e., by the force interactions between grains not related to their motion with respect to each other). For low-density snow, $\lambda \sim 0$ and $\omega_r \approx \gamma_r$, while $\Sigma_2 = \Sigma_3 = -p \sim 0$. In this case Eqs. (5) and (6) lead to $\eta' = 2\eta/3$.

For plastic deformation, one can envisage the following non-linear analogues of Eqs. (6):

$$p = F(\omega_p)\ , \qquad T_1 = -4G(\gamma_p)\ . \qquad (7)$$

The apparent viscosity of ice-grain rearrangement η and functions $F(\omega_p)$ and $G(\gamma_p)$ in Eqs. (6) and (7) (to be

determined below) are the principal rheological characteristics of the ice compact, relating the macroscopic behavior to the processes occurring on the microstructural level. By definition, the vertical stress Σ_1 is equal to $-p_I$ with its deviatoric part T_1 given identically by Eqs. (6) or (7). Based on Eqs. (3)-(7), these conditions can be written as

$$p_I = F(\omega_p) + 2(3-\lambda)G(\gamma_p)\,, \qquad \eta\dot{\gamma}_r = G(\gamma_p) \quad (8)$$

Together with Eqs. (4), they deliver a general form of the snow/firn densification model with respect to ω and x.

The snow/firn structure, including the effects of pressureless sintering in grain bonding, and the densification mechanisms by ice-particle rearrangement and creep are sequentially considered in the following subsections in order to explicitly transform Eqs. (8) into a complete physical model.

2.2. Densification stages and snow/firn structure description

Hereafter we conventionally introduce the two successive stages of snow/firn densification and distinguish them for clarity after [8, 9] as "snow" and "firn", respectively. However, in contrast to previous studies, we assume after [60] that the first (snow) stage, dominated by ice particle restacking, is simultaneously influenced by a gradual increase in the plastic strain of grains. The firn (consolidated snow) stage starts when particle rearrangement ceases at the closest, dense packing and is controlled only by grain dislocation creep under growing overburden pressure. In this context, a shift of the snow-to-firn transition (critical point) to greater depths and higher relative densities can be expected.

The number of contacts (bonds) per grain (coordination number, Z) is one of the principal microstructural characteristics of snow/firn build-up. The increase in Z with density during the snow densification stage occurs primarily as a result of ice-grain restacking. In accordance with ice core measurements [4, 7], snow structure modeling [32], and direct simulations of microscopic snow densification [41], we assume after [2] that Z in snow is a linear function of the relative density ρ,

$$Z = Z_0\rho/\rho_0\,. \quad (9)$$

The subscript "0" designates the critical values at the critical depth of dense packing, where particle rearrangement stops and the firn stage begins.

Consistently, firn densification is realized to occur by centre-to-centre approach of ice crystals due to the dislocation creep without sliding. Following [10], we represent the firn structure on average as a random dense packing of incompressible monosize grains of equivalent-sphere radius R and use a linear approximation of the cumulative particle radial distribution function (RDF) with relative slope C. Further, in accordance with Arzt's approach (see Fig. 2), the development of the ice-grain structure due to dislocation creep is described as the concentric expansion of centre-fixed particles with the current 'fictitious' equivalent-sphere radius R' measured in units of R. The basic shape of the plastically deformed grain bodies is thus the sphere of relative radius R'' truncated by the developing and newly-formed contact faces with the free surface fraction s. The coordination number in firn is then

$$Z = Z_0 + C(R''-1)\,. \quad (10)$$

The critical value Z_0 of the coordination number for random dense packing and the slope C of the radial distribution function estimated in [10] for monosize-sphere powders are ~ 7-7.5 and ~ 15.5. Accordingly, R' is expressed via the relative density ρ, and R'' is related to R', linking Z to ρ (see Appendix A).

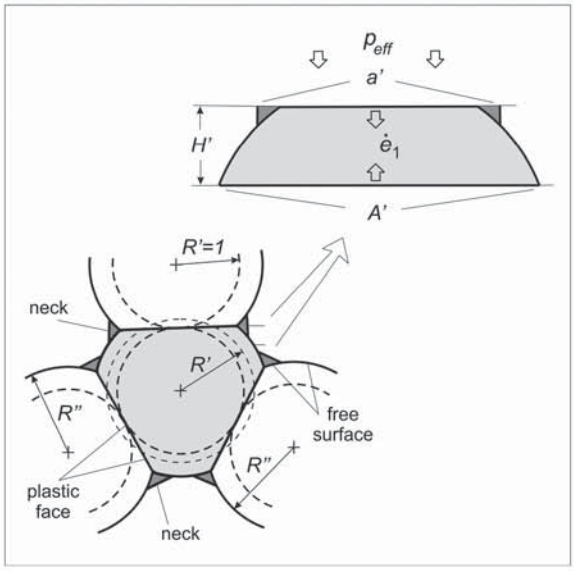

Figure 2: Modification of Arzt's geometric scheme [10] of ice-grain compaction by dislocation creep coupled with neck formation around plastic faces due to diffusive water-vapor transport. Inset: Deformation of a single spherical contact domain on a reference grain.

Although the restacking and dislocation creep of grains are considered to be the major pressure-sintering (densification) mechanisms in snow and firn, the water-vapor transport and other pressureless-sintering processes in the granular ice material at relatively high homologous temperature may also contribute to grain bonding and neck formation [1, 2, 35], enlarging the grain contact faces and slowing the rates of plastic deformation. To account for these effects, Arzt's geometrical description of the firn structure is extended to the snow stage where the creep of ice particles is subservient in densification and the cumulative plastic strain of grains is, at least in part, annihilated by grain rearrangement. Thus, without any loss of generality it can be assumed that the area fraction of plastically

formed intergranular contacts $1 - s$ in snow is negligibly small, that is, $s = R' = R'' = 1$ with Eq. (9) substituted for Eq. (10) at $\rho < \rho_0$. A new microstructural characteristic of the snow/firn build-up, the bonding factor ζ, is then introduced to describe the fraction of grain surface not consumed by the plastically formed contacts but occupied by excess neck volume (see Fig. 2) created due to pressureless sintering. The remainder of the reference grain surface exposed to voids $(1 - \zeta)s$ is shared among the contact domains which can be realized on average as spherical segments with flat bases A' (Fig. 2). This generalized geometry of snow/firn structure is qualitatively described in Appendix A. The equations for R'', s, the mean relative bond area a', and the average area of the contact-segment base A' (i.e., $a = a'/R^2$ and $A = A'/R^2$ in units of R^2) are derived in the appendix. The fraction of grain surface area involved in the grain bonds s_b is also obtained to link these microstructural characteristics via R' to ρ. The critical density ρ_0 is shown to be uniquely expressible in terms of Z_0 and C.

Observations [1, 2] revealed that ice-grain bond development is counterbalanced to a large extent by grain-boundary sliding in snow, resulting in a constant mean bond area a_0. This means, as confirmed by measurements [4, 7, 9], that in the snow stage, the grain bond fraction s_b is a linear function of Z or ρ (see Eq. (9)). As shown in Appendix A, to satisfy the condition $a = a_0$, the bond parameter ζ must also be a linear function of Z, i.e.,

$$\zeta = \zeta_0 Z/Z_0 \,. \tag{11}$$

The critical value ζ_0 uniquely determines a_0. Eq. (11) is extended below to the firn stage and will be validated on the basis of ice-core data. Finally, only three microstructural parameters Z_0, C and ζ_0 of dense packing control the evolution of snow/firn build-up with increasing density.

In relation to the specific surface area, the present approach is quantitatively equivalent to the snow/firn structural representation of ice crystal agglomerates suggested by Arnaud and coworkers in [8, 9]. In this framework, in the snow stage, ζ is equal to the mean fraction of the grain surface occupied by bonds and can thus be regarded as a measure of agglomeration. However, Arnaud's approach assumes that ice crystal aggregates initially have zero contact faces at the snow-to-firn transition, precluding direct incorporation into the ice grain rearrangement scheme [2], which is essentially based on grain sliding over developed interfaces. In contrast, Eqs. (9)-(11) explicitly introduce an average description of intergrain contacts that is continuously consistent in snow with Alley's model [2] and allows direct application of Arzt's theory [10] for firn densification.

Considering pressureless sintering as an important factor in the formation of intergrain contacts, we still assume that the transportation of extra mass of ice to necks does not change the density or R'' substantially. Hence, Eq. (10) for pressure sintering [10] in firn remains valid without substitution of R' for R'' as suggested in [29]. At the same time, it should be noted that the polydispersity of natural snow and the primary redistribution of ice across the grain surface in the snow stage can result in a denser closest packing with higher Z_0 and much higher RDF slope C than the values conventionally accepted for spherical monosize powders [10]. Thus, Z_0 and C should be regarded as tuning model parameters in addition to ζ_0.

2.3. Alley approximation for snow densification by grain-boundary sliding

Alley's theory [2] of the snow densification by grain-boundary sliding gives

$$\frac{1}{\rho}\frac{d\rho}{dt} = 3\omega_r = \frac{4\delta R\Gamma(Z)}{3\nu r^2 \rho^2 Z} p_l \,,$$

where δ and ν are the grain-bond thickness and viscosity, respectively. R is the mean equivalent-sphere radius of grains, and r is the mean bond radius. The coefficient $\Gamma(Z)$ can be expressed as a linear function of the coordination number (or density via Eq. (9)), decreasing from 1 to 0 as Z increases from 0 to Z_0.

Comparison of this relation to the general equations (1), (4), and (8), neglecting the plasticity effect (i.e., $x \sim 1$ and $\lambda \sim 0$) yields the following explicit expression for η:

$$\frac{1}{\eta} = \frac{8\pi\delta\,\Gamma(Z)}{3\nu a R \rho^2 Z} \,,$$
$$\Gamma(Z) \approx \left[\left|1 - Z/Z_0\right| + \left(1 - Z/Z_0\right)\right]/2 \,. \tag{12}$$

Here, by definition, $a = \pi r^2/R^2$ and in accordance with [1], a can be regarded as a constant value $a = a_0$ in Eqs. (12).

2.4. Plastic deformation in ice compact

Densification by dislocation creep occurs under external pressure p, which is transformed in the ice skeleton to an effective pressure p_{eff} acting on grain contacts. On average, for uniformly distributed forces, it is conventionally accepted (e.g., [10, 50]) that $p = \rho a Z p_{eff}/4\pi$. However, according to Gubler [36], the external stresses imposed on the polydisperse ice grain structure are conducted by "fundamental units" (groups of grains) through "force chains" (series of single force-bearing grains). As not all gains are stressed and undergo the creep, the effective pressure on the grains controlling macroscopic deformation, particularly in snow and low-density firn, is higher than the value averaged over all ice particles. Gubler's measurements [36] of the force-chain lengths for coordination numbers of 3-10 predict an extra increase in p_{eff} in inverse proportion to Z. Phenomenologically, this can be accounted for by introducing an additional enhancement factor Z/Z_0 into the above correlation between p and p_{eff}.

In the framework of Arzt's description [10] of the geometrical granular ice structure, it is assumed here that in plastic deformation, ice is squeezed from under each contact area a' on a reference grain by power-law creep of the uniaxially compressed contact-segment layer (see Fig. 2, inset). The central part of the grain is subjected to uniform forcing from all surrounding segments and is thus in hydrostatic equilibrium. The rheological law for ice as a non-linear viscous incompressible body, relating effective strain rates $\dot{e}_0$ to effective stresses τ_0, is given by

$$2\mu\dot{e}_0 = \tau_0^{\alpha} , \tag{13}$$

where α is the creep index and μ is the coefficient of non-linear viscosity.

The problem of plastic deformation of the contact segments under effective pressure is considered in Appendix B. The obtained solution transforms the ice flow law (13) into a relationship between p_{eff} and ω_p, and the correlation between p and p_{eff} leads directly to the following expression of $F(\omega_p)$ in Eqs. (7) and (8):

$$p = F(\omega_p) \equiv \frac{\sqrt{3aA}\rho Z^2}{4\pi Z_0}\left\{\frac{2\sqrt{3}\pi\mu R'}{asR''}\left[1-(1-\zeta)s\right]\omega_p\right\}^{1/\alpha} . \tag{14}$$

Eq. (14) differs from its analogue proposed in [11] and implies a substantial decrease in densification rates due to bonding effects and a reduction in the free surface fraction s. It should be noted that a higher value of coordination number (e.g., attained at pore close-off) might be more appropriate for use in the correction factor Z/Z_0 in Eq. (14) instead of Z_0. A certain renormalization of non-linear viscosity μ introduced by Eq. (13) can thus be expected.

The general equations (6)-(8) demonstrate the importance of deviatoric stresses and strain rates in the densification of granular ice under uniaxial compression. Fundamental units in which grains respond to deviatoric stresses by relative sliding with minimum resistance do not play a significant role in the macroscopic plasticity. Only the relatively small fraction of force-bearing chain grains with developed necks which are aligned with the principal axes of deformation is fully involved in the deviatoric strains (stretching and/or constriction) by creep. A high-density asymptotic approximation [61] can be introduced for deviatoric stresses to be multiplied, as in the case of effective pressure, by the enhancement factor Z/Z_0 with additional correction $\varepsilon\rho$ to account for a reduced number of deviatorically deformed force-bearing chains, i.e.,

$$T_1 = -4G(\gamma_p) \equiv -\frac{2\varepsilon\rho^2 Z}{\sqrt{3}Z_0}\left(2\sqrt{3}\mu\gamma_p\right)^{1/\alpha} , \tag{15}$$

where ε is the snow/firn structural characteristic assumed to be a small value.

Eqs. (14) and (15) together with Eq. (11) and other microstructural characteristics determined in Appendix A are equally valid in snow for $\rho < \rho_0$ at $R' = R'' = 1$ and in firn for $\rho > \rho_0$ with Z given by Eqs. (9) and (10), respectively.

2.5. Physical model for snow/firn densification rates

Simultaneous equations (4), (8), (12), (14), and (15) form a theoretical basis for physical modeling of the snow/firn densification process. Substituting Eqs. (4), (14), and (15) into the first of Eqs. (8) for both snow and firn stages yields

$$p_I = \frac{\sqrt{3aA}\rho Z^2}{4\pi Z_0}\left\{\frac{2\sqrt{3}\pi\mu R'}{asR''}\left[1-(1-\zeta)s\right]\left[1-(1-\lambda)x\right]\omega\right\}^{1/\alpha} + \frac{\varepsilon\rho^2 Z(3-\lambda)}{\sqrt{3}Z_0}\left[2\sqrt{3}\mu(1-x)\omega\right]^{1/\alpha} . \tag{16}$$

The principal novelty of this relation is that it extends now to plastic deformation in snow, accounting for the dilatancy effects and ice-grain rearrangement described by parameters λ and x, respectively. Although an accurate estimate of the value of ε in Eq. (15) is not available, the bubbly ice densification theory [61] predicts that the average pressure p in the ice matrix is close to the overburden pressure p_I. Hence, the influence of the deviatoric stresses (second term) in Eq. (16) is expected to be rather small, if not negligible. In contrast, the deviatoric stresses and parameter ε play a key role in the second of Eqs. (8), which relates the deviatoric strains of different origins in snow for $\rho < \rho_0$. In combination with Eqs. (4), (12), and (15), this equation can be rewritten as

$$x\omega = k_r\frac{\Gamma(Z)}{R}\left[\mu\omega(1-x)\right]^{1/\alpha} ,$$
$$k_r = \frac{16\left(2\sqrt{3}\right)^{1/\alpha}\pi\varepsilon\delta}{3\sqrt{3}va_0Z_0R_s} . \tag{17}$$

Here $\bar{R} = R/R_s$ is the relative grain size normalized by the initial grain radius R_s at the ice-sheet surface, and k_r is a new complex constant of the grain rearrangement rate.

Simultaneous equations (16) and (17) are the principal part of the snow densification model, relating the densification rate ω and deviatoric ice-grain rearrangement ratio x to the overburden pressure p_I and microstructural snow properties. It is important to note that in the general case of $\lambda > 0$, even in low-density snow, when $x \to 1$, these equations can not be reduced to an Alley-type model [2] simply by excluding the product $\mu\omega(1-x)$.

Hereinafter a power approximation is introduced for the dilatancy parameter as a function of relative density

$$\lambda = \left(\frac{\rho - \rho_{\min}}{\rho_0 - \rho_{\min}} \right)^{\beta}, \rho < \rho_0, \qquad (18)$$

where β is the dilatancy exponent and $\rho_{min} \sim 0.3$ is the minimum surface-snow (threshold) density below which the dilatancy effects are assumed to be negligible.

In snow, $R' = R'' = 1$, and Eq. (9) for coordination number Z completes the model (16)-(18). In firn, $\lambda = 1$ and $\Gamma(Z) \equiv 0$ for $\rho > \rho_0$ ($Z > Z_0$). Correspondingly, Eq. (17) reduces to $x = 0$, and Eq. (16) determines directly the densification rate ω at Z given by Eq. (10). In both stages, the bonding factor ζ is given by Eq. (11). All other microstructural characteristics are specified in Appendix A.

The developed physical description of the snow/firn densification process involves three geometrical parameters (Z_0, C, ζ_0), two grain interaction parameters (β, ε), and two ice properties (μ, k_r), all of which should be constrained or validated by ice core density measurements and texture analyses.

3. Model constraining and validation

3.1. Snow/firn structure characteristics

Ice-grain connectivity in snow and firn is quantitatively described by the coordination number Z and the bond area fraction s_b. Alley and Bentley [4] convincingly demonstrated, on the basis of a stereological study of BC and UpB ice cores from the Siple Coast, West Antarctica, and data from Site A, Greenland [5], that these microstructural characteristics are well correlated with density for various types of snow and firn. Later measurements by Arnaud [7] of East Antarctic ice cores from Vostok Station and from two sites (KM105 and KM200) at 105 and 200 km along the traverse from Mirny observatory to Vostok, also confirmed this conclusion. The details of these and all other sites discussed in the present paper are listed in Table 1.

In the proposed model, $Z(\rho)$ is expressed by Eqs. (9) and (10) in snow and firn, respectively. As detailed in Appendix A, this relationship is controlled by the two geometrical parameters Z_0, C, and by the resultant critical density ρ_0. Fig. 3 compares the theoretical curves with available ice core data. The observed general trends and the scatter of the measurements fall within the minimum uncertainty range of the critical coordination number of $Z_0 = 6.5$-8.0, and the slope of the radial-distribution function is constrained to the expected enhanced values of $C = 40$-60 increasing with increase in Z_0. Importantly, for the Vostok and KM200 ice cores, representing two climatic extremes of low temperature with mild wind and higher temperature with strong wind (see Table 1 and [46]), the coordination numbers in the firn stage in Fig. 3b are systematically lower at Vostok (consistent with curve 1 for $Z_0 = 7$, $C = 40$) than at KM200 (e.g., curves 2 and 3 for $Z_0 = 7.5$-8, $C = 50$-60). The critical density, as an increasing function of Z_0 and C (see Appendix A), ranges respectively from $\rho_0 = 0.704$ to 0.754, and in agreement with the observational data, the slope of the theoretical curves of $Z = Z(\rho)$ in Fig. 3 changes at $\rho = \rho_0$ with switching from Eq. (9) to Eq. (10). These values of ρ_0 are substantially higher than the relative density (ca. ~0.6) of the first uppermost bend point of the sharp decrease in densification rates found in the density profiles by Anderson and Benson [6] and suggested to be the boundary between the snow and firn stages.

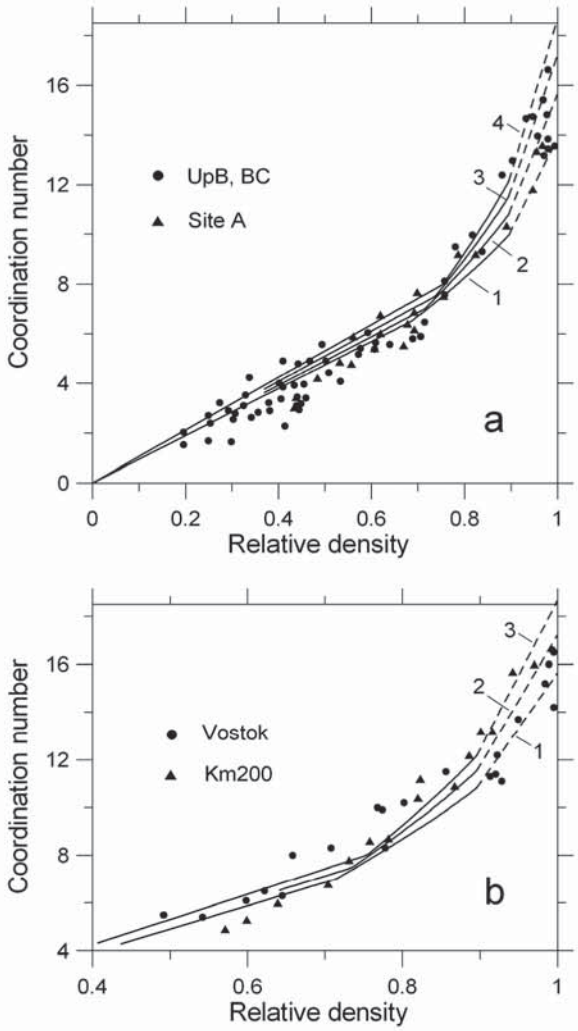

*Figure 3: Coordination number versus relative density (symbols) for ice cores from (**a**) UpB, BC, and Site A [4, 5] and (**b**) Vostok and KM200 [7] compared to model approximations (solid lines) for various ice-core structures specified by critical microstructural parameters: (**a**) (1) $Z_0 = 6.5$, $C = 30$, (2) $Z_0 = 7$, $C = 40$, (3) $Z_0 = 7.5$, $C = 50$, (4) $Z_0 = 8$, $C = 60$; (**b**) (1) $Z_0 = 7$, $C = 40$, (2) $Z_0 = 7.5$, $C = 50$, (3) $Z_0 = 8$, $C = 60$.*

Another important peculiarity is that, even for relatively small variations of Z_0 and C, the corresponding changes in ρ_0 are sufficiently large to cause a noticeable shift of the critical depth h_0 at which the transition from snow to firn occurs. These features will be addressed in more detail below.

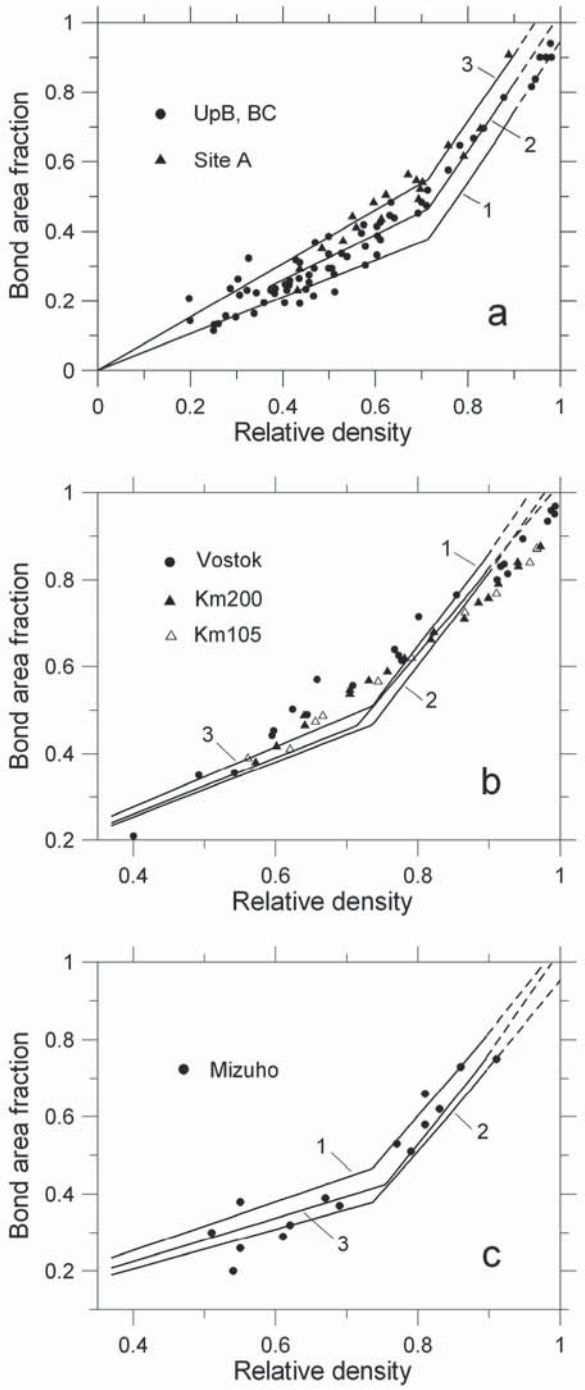

Figure 4: Bond area fraction versus relative density (symbols) for ice cores from ***(a)*** *UpB, BC, and Site A [4, 5],* ***(b)*** *Vostok, KM200, and KM105 [7, 9], and* ***(c)*** *Mizuho [54] compared to model predictions (solid lines) for various ice core structures specified by different critical bonding factors:* ***(a)*** $Z_0 = 7$, $C = 40$, (1) $\zeta_0 = 0.4$, (2) $\zeta_0 = 0.5$, (3) $\zeta_0 = 0.6$; ***(b)*** (1) $Z_0 = 7$, $C = 40$, $\zeta_0 = 0.5$, (2) $Z_0 = 7.5$, $C = 50$, $\zeta_0 = 0.5$, (3) $Z_0 = 7.5$, $C = 50$, $\zeta_0 = 0.55$; ***(c)*** (1) $Z_0 = 7.5$, $C = 50$, $\zeta_0 = 0.5$, (2) $Z_0 = 7.5$, $C = 50$, $\zeta_0 = 0.4$, (3) $Z_0 = 8$, $C = 60$, $\zeta_0 = 0.45$.

The deduced estimates of Z_0 and C can be used to constrain the critical value of the bonding factor ζ_0 in Eq. (11) on the basis of bond-area fraction measurements s_b. As shown in Appendix A, the mean contact area a is directly related to ζ (i.e., ζ_0), and s_b is determined as $aZ/(4\pi)$. Calculations by Eq. (11) performed at $Z_0 = 7$ and $C = 40$ are also in general agreement with the grain-boundary surface measurements [4] for $\zeta_0 = 0.5 \pm 0.1$ (see Fig. 4a). These estimates correspond to mean relative bond area of $a_0 = 0.83 \pm 0.15$ in snow and a relative bond radius of 0.52 ± 0.05, which is also close to observations [1, 2]. Figs. 3a and 4a and additional computational experiments indicate lower values of $Z_0 \sim 6.5$-7 and higher values of $\zeta_0 \sim 0.6$ for Site A core, while the structure of the BC core is characterized by $Z_0 \sim 7$ and $\zeta_0 \sim 0.5$ at $C = 40$. Snow/firn texture analyses of Antarctic ice cores from Vostok Station, KM105, and KM200 [7-9] are similarly consistent among the cores (Fig. 4b) with a possible range of $\zeta_0 \sim 0.5$-0.55 at $Z_0 = 7$-7.5 and $C = 40$-50. Ice-grain specific surface measurements [54] on the ice core from Mizuho Station, after transformation into bond area fraction values, suggest ζ_0-values of ~ 0.45-0.5 (Fig. 4c) and confirm a tendency to denser firn structures with $Z_0 \sim 7.5$-8 and $C \sim 50$-60 under the strong wind conditions typical for Mizuho area [74].

As summarized in Table 2, for the 6 sites on Antarctic and Greenland ice sheets which cover a wide range of present-day ice-formation conditions, the microstructural parameters Z_0, C, and ζ_0 are reliably constrained within ±10% uncertainty limits by direct stereological observations of ice cores. More accurate tuning is needed and can be performed on the basis of ice core density measurements in order to obtain a better understanding of the impact of weather and climate on the characteristics and evolution of the snow/firn structure.

3.2. Modeling the density-depth profile

Aside from the geometrical characteristics of the microstructure, no other parameters of the snow/firn densification model can be measured directly and/or separately in laboratory experiments. The best and, most probably only, way of constraining the model further is to infer the parameter values by fitting theoretical density-depth profiles to ice core density measurements.

In the general case, the non-stationary distribution of the relative density ρ of snow/firn deposits on an ice sheet versus depth h is governed by the basic equation (1) where the particle derivative in a quasi-one-dimensional approximation is expressed as

$$\frac{d}{dt} = \frac{\partial}{\partial t} + w\frac{\partial}{\partial h} \ .$$

Here, w is the downward vertical velocity of the porous-ice medium with respect to the ice sheet surface. The

compression rate ω in Eq. (1) is related by Eqs. (16) and (17) to the load pressure

$$p_l = g\rho_i \int_0^h \rho dh \ , \qquad (19)$$

where g is the gravity acceleration and ρ_i is the density of pure ice.

The velocity w is governed by the general mass conservation equation, which after integration with respect to h takes the form

$$\rho w = b - \frac{1}{g\rho_i}\left(\frac{\partial p_l}{\partial t} + \dot{e}_1 p_l\right) , \qquad (20)$$

as derived in Appendix C.

Here, b is the ice accumulation rate (in ice equivalent), and in accordance with [61], $\dot{e}_1$ is the rate of thinning induced by the global motion of the ice sheet. In central parts of thick polar ice sheets, this quantity is of the order of $\dot{e}_1 \sim b/\Delta$, where Δ is the ice-equivalent glacier thickness. Consequently, the last term in Eq. (20) is usually small (i.e., $\dot{e}_1 p_l /(g\rho_i) \sim \dot{e}_1 h \sim bh/\Delta << b$), representing a second-order correction. The latter correction may become substantial in marginal areas, ice streams, and mountain glaciers at high flow rates and intense global deformation when $\dot{e}_1 h /b \sim 1$ within the snow/firn densification layer. However, in most of such cases the quasi-one-dimensional approximation breaks down and more general ice flow schemes and snow/firn rheological models should be considered.

Table 1: Site locations and ice-formation conditions.

Drilling site	Location	ρ_s*	T (10 m), °C	b, cm yr^{-1}	ρ_i, kg m^{-3}	Group**	Reference
Dôme du Goûter	45°55'N, 6°55'E	0.43	-10	330	918	H	[30]
Ushkovsky	59°04'N, 160°28'E	0.38	-15.8	59	919	H	[68]
H72	69°12'S, 41°05'E	0.41	-20.3	34.5	919	H	[57]
KM60	67°05'S, 93°19'E	0.46	-20.8	50.3	920	H	[46, 47], this work
Milcent	70°18'N, 45°35'W	0.38	-22.3	54.4	920	H	[53]
KM105	67°26'S, 93°23'E	0.46	-24.5	34.1†	920	H	[46, 47], this work
Site 2	76°59'N, 56°04'W	0.375	-25	42.4	920	L	[44]
BC	82°54'S, 136°40'W	0.33	-26.5	9	920	L	[4]
KM140	67°45'S, 93°39'E	0.485	-27	43.9†	920	H	[46, 47], this work
B25	79°37'S, 45°43'W	0.38	-27	15.2	920	L	[31]
Byrd	80°00'S, 120°00'W	0.39(0.41)	-28.7	17.4	921	L	[34]
Site A	70°45'N, 35°58'W	0.37	-29.5	29	921	L	[5]
Crete	71°07'N, 37°19'W	0.38	-29.7	29.3	921	L	[53]
KM200	68°15'S, 94°05'E	0.49	-30.5	28.7†	921	H	[46, 47], this work
Summit	72°35'N, 37°38'W	0.42	-31.7	23	921	L	[66, 67]
Mizuho	70°42'S, 44°20'E	0.44	-33	7.5	921	H	[54, 74]
Pionerskaya	69°44'S, 95°30'E	0.47(0.46)	-39	19.4	922	H	[46, 69], (K.E. Smirnov, pers. com.)
Vostok-1	72°08'S, 96°35'E	0.42(0.41)	-47	8.9	923	L	[46], (K.E. Smirnov, pers. com.)
Komsomolskaya	74°06'S, 97°30'E	0.39(0.36)	-53.8	6.9	923	L	[47]
EPICA DC	75°06'S, 123°21'E	0.37	-54.5	2.7	923	L	[28, 59], this work
Dome Fuji	77°19'S, 39°42'E	0.39	-57‡	3.2‡	924	L	[21, 42, 75], this work
Vostok	78°28'S, 106°48'E	0.38(0.35)	-57.5‡	2.15‡	924	L	[27, 47, 48]

* Values in parentheses are direct surface snow density measurements in the upper 20-50-cm layer
** See subsection 4.1 for explanations
† Values corrected for the site movement and accumulation-rate changes along the ice flow line
‡ Values additionally constrained and verified through ice flow modeling [40, 62, 72]

Table 2: Microstructural parameters and densification characteristics deduced from ice core data.

Drilling site	Z_0	C	ζ_0	β	ρ_0	h_0, m	h_{off}, m	t_{off}, kyr	B_t (B_h)	Group
Dôme du Goûter	7.5	50	0.55	9.5	0.736	30.8	64.5	0.018	2.29(2.30)	H
Ushkovsky	7.5	50	0.54	9.5	0.736	24.0	52.6	0.072	2.34 (2.36)	H
H72	7.5	50	0.56	9	0.736	24.6	54.9	0.116	2.42 (2.44)	H
KM60	8	60	0.52	9	0.754	26.9	57.1	0.084	2.27 (2.32)	H
Milcent	7.5	50	0.58	8.5	0.736	29.6	65.1	0.087	2.46 (2.49)	H
KM105 †	7.5	50	0.55	9.5	0.736	27.0	61.4	0.132	2.44 (2.44)	H
Site 2	7	40	0.57	8	0.714	29.6	68.4	0.116	2.58 (2.57)	L
BC †	7	40	0.53	6	0.714	22.2	49.7	0.391	2.54 (2.57)	L
KM140	7.5	50	0.56	10	0.736	30.1	69.0	0.116	2.47 (2.46)	H
B25	7	40	0.54	7	0.714	24.8	57.0	0.268	2.56 (2.56)	L
Byrd	7	40	0.54	7.5	0.714	26.4	61.3	0.253	2.57 (2.56)	L
Site A †	6.5	40	0.61	8	0.704	31.3	77.3	0.191	2.81 (2.75)	L
Crete	7	40	0.5	7.5	0.714	29.7	69.6	0.170	2.53 (2.5)	L
KM200 †	7.5	50	0.53	9.5	0.736	29.6	68.3	0.176	2.46(2.45)	H
Summit	7	40	0.59	6	0.714	32.9	73.4	0.227	2.65 (2.66)	L
Mizuho †	8	60	0.48	10	0.754	23.4	51.2	0.506	2.31 (2.35)	H
Pionerskaya	7.5	50	0.53	8	0.736	35.9	81.4	0.308	2.52 (2.53)	H
Vostok-1	7	40	0.5	7	0.714	38.3	90.5	0.732	2.65 (2.63)	L
Komsomolskaya	6.5	40	0.55	5.5	0.704	49.0	116.9	1.203	2.92 (2.90)	L
EPICA DC	6.5	40	0.62	4	0.704	43.9	101.0	2.626	3.0 (3.01)	L
Dome Fuji	6.5-7	40	0.53-0.6	4-4.5	0.704-0.714	47.1-49.5	110.1-108.2	2.427-2.382	2.88 (2.90)	L
Vostok †	7	40	0.5	3.5	0.714	44.8	97.5	3.173	2.73 (2.78)	L

† Microstructural characteristics are constrained by direct stereological measurements in subsection 3.1

Eq. (1) is solved starting from a given surface snow density ρ_s

$$\rho|_{h=0} = \rho_s \,. \tag{21}$$

As the snow/firn densification is a temperature-controlled process, the rheological parameters μ and k_r in Eqs. (16) and (17) (the principal temperature-dependent properties of ice) are conventionally assumed to be Arrhenius-type functions of absolute temperature T (in K):

$$\mu = \mu^* \exp\left[\frac{Q_p}{R_g}\left(\frac{1}{T}-\frac{1}{T^*}\right)\right], \qquad k_r = k_r^* \exp\left[\frac{Q_r}{R_g}\left(\frac{1}{T^*}-\frac{1}{T}\right)\right]. \tag{22}$$

Here, Q_p and Q_r are the activation energies of plastic deformations in ice and grain rearrangement by boundary sliding, respectively. The parameters marked with an asterisk denote those at the reference temperature T^*, and $R_g = 8.314$ J (mol K)$^{-1}$ is the gas constant.

The ice crystal size is often characterized by the mean crystal area A_c measured in ice-core thin sections. For normal grain growth, it is well established that at fixed temperature, A_c is a linear function of time. Accordingly, in a variable climate, we have

$$dA_c/dt = k_c\,, \quad A_c|_{h=0} = A_{cs}\,; \qquad k_c = k_c^* \exp\left[\frac{Q_c}{R_g}\left(\frac{1}{T^*}-\frac{1}{T}\right)\right], \tag{23}$$

where A_{cs} is the ice crystal size at the ice sheet surface, k_c is the growth rate constant, and Q_c is the activation energy of crystal growth. A review and detailed analysis of available data for Antarctic ice cores [47] suggest values of $Q_c = 45.6$ kJ mol^{-1} and $k_c^* = 3.9\cdot10^{-4}$ mm^2 yr^{-1} at a reference (Vostok Station) temperature of

$T^* = 215.7$ K. These estimates and a constant averaged crystal size at the glacier surface, $A_{cs} \approx 0.7$ mm^2, are assumed in our study in Eqs. (23) after [47] to simulate the relative ice-grain radius $\overline{R} = \sqrt{(A_c / A_{cs})}$ in Eq. (17).

The model (1) and (16)-(23) governs the non-stationary density-depth distribution in the dry snow/firn stratum on an ice sheet. These equations should be coupled with the heat transfer equation to account for temporal changes in temperature (e.g., [33]). Water-vapor transport may also become important as a mass transfer mechanism in Eq. (1) at high temperature gradients (e.g., [37, 58, 64]). The model describes the densification process above a certain depth h_{off} at which atmospheric air becomes trapped in the ice matrix and firn is transformed into bubbly ice. The prediction of pore closure is regarded as a separate problem that is beyond the scope of the present paper. In the applications considered below, based on [47, 51, 52], a linear empirical correlation between the close-off density ρ_{off} and firn temperature is conventionally employed, as given by

$$\rho_{off} = 0.9 - 5.39 \cdot 10^{-4} (T - 235) . \qquad (24)$$

An interactive computer system was developed to solve Eqs. (1), (16), and (17) completed by Eqs. (18)-(24) and simulate density-depth profiles in the snow/firn layer of an ice sheet. The program allows ready adjustment of model parameters and fitting of the computational predictions to ice core density measurements.

3.3. Model constraining and ice core density data analysis

A series of preliminary computational tests was performed in order to study the sensitivity of the densification model to the rheological parameters ε, k_r, μ, and the dilatancy exponent β. They revealed that largely identical density-depth profiles can be obtained for a range of small values of ε in Eqs. (15) and (16), assuming that the non-linear viscosity decreases with increasing ε. Thus, the correction factor is fixed at $\varepsilon = 0.1$, corresponding to an ice pressure p approximately 7% lower than the load pressure p_l at the close-off depth, similar to the predictions for bubbly ice [61]. It was also confirmed that, in accordance with the physical meaning, three other parameters k_r, β, and μ selectively control the density distribution in the respective depth intervals of near-surface snow, an intermediate zone of ice-grain rearrangement noticeably influenced by dilatancy effects, and the firn stage of densification by dislocation creep.

A total of 22 ice core density profiles were selected for model constraining and validation. They are mainly from the Antarctic and Greenland ice sheets (Table 1) and cover a temperature range of almost 50 °C (–57 to –10 °C), ice accumulation rates of 2.2 to 330 cm yr^{-1}, and various weather (wind) conditions (e.g., [46]). Among them, density measurements for the 6 ice cores with the observed textures (Vostok, Mizuho, Km200, Site A, BC, and KM105) form a representative uniformly distributed set of data. These basic experimental profiles, plotted by open circles in Figs. 5a-f, are used to constrain the temperature-dependent rheological properties k_r, and μ, and the index β. Other density profiles from ice cores in Table 1 are employed to validate the model and to study the development of the snow/firn structure during the densification process under different climatic and weather conditions.

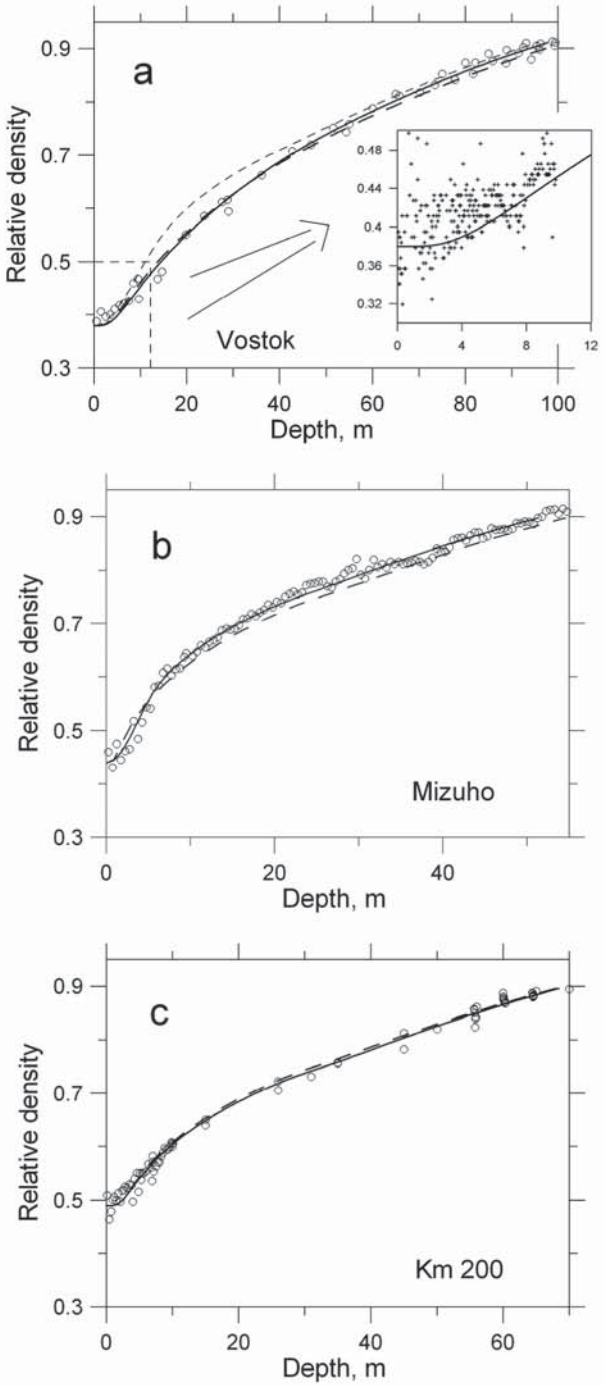

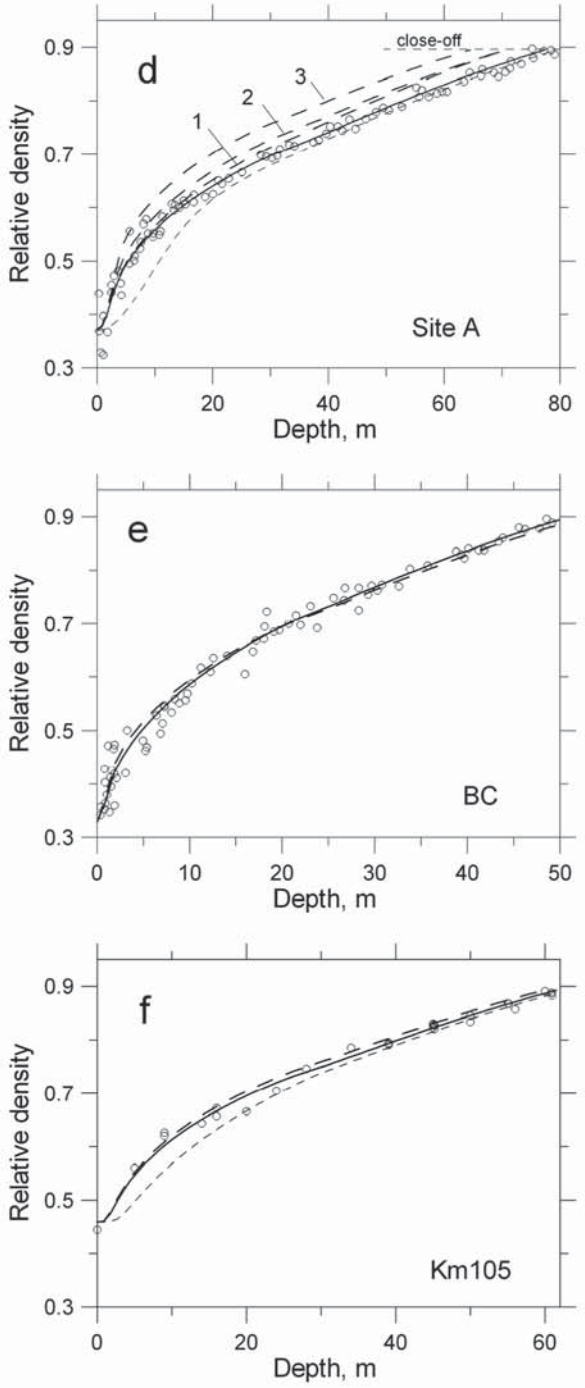

*Figure 5: Basic ice-core density profiles (open circles) from six Antarctic and Greenland sites (**a**) Vostok, (**b**) Mizuho, (**c**) KM200, (**d**) Site A, (**e**) BC, and (**f**) KM105 with model predictions (solid lines) fitted to constrain rheological parameters. Dashed lines in (**a**, **b**, **c** and **e**, **f**) are the profiles simulated at recommended parameters from Table 3. Results in (**d**) are compared with those for L- and H-microstructures of (1) Crete, (2) Milcent, and (3) Mizuho ice cores (dashed lines). Dotted lines in (**a**) and (**f**) represent profiles calculated for alternative values of β (increase from 3.5 to 7 in (**a**) and decrease from 9 to 6 in (**f**)), dotted line in (**d**) corresponds to reduced apparent activation energy of Q_r = 40 kJ mol^{-1} of ice-grain rearrangement.*

In all simulations it is assumed that snow/firn strata have been formed at constant present-day (or mean Holocene) temperatures, accumulation rates, and relative surface snow densities ρ_s (Table 1), and the density-depth relationships are modeled as quasi-stationary distributions. If several measurements of accumulation rates at a certain site are available for a number of periods [46], the weighted mean value is calculated, corrected if necessary for site movement along the ice flow line [47]. It should be emphasized that the surface density ρ_s is not regarded as a tuning parameter, but is understood as a long-term mean of the near-surface snow layer consistent with the general trends of the density-depth profiles extrapolated to the surface [46]. In some cases, these "effective driving" densities can differ slightly from the snow densities measured directly in the 20-50 cm thick surface layer (Table 1, values in parentheses). The use of these present-day values may slightly perturb the simulated density-depth curves within the upper 3-6 meters, but does not change the general conclusions. The strain rates of vertical thinning caused by "external" ice motion are small in most cases, and $\dot{e}_1 = 0$ in Eq. (20). The exceptions are the ice cores from the Dôme du Goûter glacier at the summit of Mont Blanc [30] and the Gorshkov ice cap in the crater of the Ushkovsky volcano at Kamchatka [68].

Computational experiments indicate that plastic deformation of ice grains in snow becomes important at effective pressures p_{eff} at intergrain contacts substantially greater than ca. ~0.1 MPa, the threshold value at which the power-law creep with constant exponent α takes place in the densification process [48, 61]. To be consistent with these works, a value of $\alpha = 3.5$ is employed here. Sensitivity tests confirmed that variations of α within its uncertainty range (2.5 to 4) can be compensated for by corresponding changes in the non-linear viscosity μ. The simulated density-depth curves obtained through minimizing the standard deviations from ice core measurements at Vostok, Mizuho, Km200, Site A, BC, and KM105 (Fig. 5, solid lines) are in excellent agreement with the ice core data. The corresponding best-fit values of β, k_r, and μ (at $\alpha = 3.5$) are inferred at the microstructural characteristics Z_0, C, and ζ_0 that are determined from the direct stereological observations and additionally validated (within respective uncertainty limits) through the minimization procedure. The deduced microstructural parameters are summarized in Table 2. These results suggest that the dilatancy index β varies from 3.5 to 10 over the present-day range of ice-formation conditions. In the Arrhenius relations (22), the grain-rearrangement rate constant k_r and the non-linear viscosity μ can be represented by $k_r^* = 0.022 \pm 0.003$ MPa^{-1} yr^{-1} and $\mu^* = 21 \pm 1$ MPa$^{\alpha}$ yr at the reference (Vostok) temperature of $T^* = 215.7$ K with respective activation energies of $Q_r = 70$ kJ mol^{-1} and $Q_p = 58$ kJ mol^{-1}. The only inconsistency is observed in the deduced (best-fit) k_r^* value for the

Mizuho ice core, which is a third of the mean estimate. This result can be attributed at least in part to an artifact caused by a recent short-term increase in ice accumulation [74]. Overtuning may also be responsible, since even for the Mizuho core the density-depth profile simulated at the mean values of k_r^* and μ^* (Fig. 5b, dashed line) does not deviate much from the best-fit curve. The question of overtuning is also discussed in the context of sensitivity tests below.

The obtained power-creep parameters are well constrained with accuracy of a few percent and are closely coincident with the conventionally accepted activation energy $Q_p = 60$ kJ mol^{-1} and $\mu = 41\pm18$ MPa$^{\alpha}$ yr deduced at 217 K for bubbly ice densification [48]. It is also important to remember that the phenomenological enhancement factor Z/Z_0 used in Eqs. (14) and (15) renormalizes the non-linear viscosity, decreasing slightly the value, since Z_0 is substituted for a higher (unknown) coordination number at which the intergrain contact forces become uniformly distributed in the firn structure.

A noticeably lower activation energy of 41 ± 2 kJ mol^{-1} was previously found for ice-grain rearrangement [2], consistent with the assumption that grain sliding may be controlled by molecular diffusion around obstacles through the intercrystalline boundary. In addition to the linear viscosity ν, the grain-rearrangement rate constant k_r defined by Eqs. (17) contains a number of possible temperature dependences, including the correction factor ε, the grain-bond thickness δ, the total contact area $a_0 Z_0$, and the initial grain size R_s [47]. This complexity may, at least in part, be responsible for the higher best-fit estimate of Q_r obtained here as an apparent activation energy. Furthermore, this treatment is the first time that k_r has been explicitly introduced and quantified to model the ice-structure repacking mechanism coupled with grain plasticity and dilatancy effects that hinder the relative motion of ice particles. These peculiarities of snow densification were not distinguished in Alley's theory [2]. In addition to boundary diffusion, grain sliding involves neck shearing by dislocation creep, quasi-liquid layer development, and other factors that may participate equally in the ice-crystal rearrangement process, increasing the activation energy. As revealed by the preliminary computations, k_r controls the densification of snow only within the upper 15-20 m of snow deposits subject to short-term climatic impacts and characterized by high natural fluctuations of density (see Fig. 5). Sensitivity tests on the associated uncertainty of the second of Eqs. (22) indicate that the snow-density profile is relatively stable with respect to changes in k_r^*, allowing for a range of 0.01-0.04 MPa^{-1} yr^{-1} without exceeding the data scatter. Correspondingly, activation energies of 55-60 to 75 kJ mol^{-1} do not contradict the measurements. However, Alley's estimate [2] appears to be too low. For example, even qualitative similarity is lost between the observational profile and the density-depth curve simulated at $Q_r = 40$ kJ mol^{-1} for Site A in Fig. 5d (dotted line). Despite the uncertainties discussed here, the deduced rheological properties of snow and firn appear to be quite reasonable and realistic. As further verification of these results, the model predictions can be compared to the ice core density data from other drilling sites listed in Table 1.

Thus, fixing the rheological parameters in Eqs. (22) as the best-fit mean values inferred on the basis of the 6 ice cores considered above (Vostok, Mizuho, Km200, Site A, BC, and KM105) and applying the deduced constraints on the snow/firn build-up, the microstructural characteristics Z_0, C, ζ_0, and the dilatancy exponent β are tuned to fit the simulations separately to each of the remainder observational density profiles. As shown in Appendix D, the best-fit density-depth curves (solid lines) match closely the ice core measurements (open circles). The corresponding estimates for the adjustable parameters (Z_0, C, ζ_0, and β) are summarized in Table 2. Although these values include uncertainties in terms of the prescribed snow/firn rheology and environmental ice-formation conditions, they are in full agreement with the direct stereological observations of the 6 basic ice cores. This result is a convincing confirmation of the validity of the constrained rheological equations (22) and demonstrates the much broader significance and utility of available ice-core structural data. The sensitivity of the simulated density-depth profiles to the values of the 4 tuning parameters is discussed in further detail in the next section.

It should be noted here that the Dôme du Goûter and Ushkovsky sites both experience windy conditions and the highest temperatures, at which surface snow melting begins in summer [30, 68]. For these ice cores, the rates of snow/firn strata thinning due to glacier motion are estimated to be $\dot{e}_1 \sim 2.7\cdot10^{-2}$ and $3\cdot10^{-3}$ yr^{-1}, respectively, and appreciably influence the downward velocity in Eq. (20). Even in such limiting cases, the model predictions are in good agreement with the measured density profiles.

4. Applications. Discussion

4.1. Impact of ice-formation conditions on snow/firn structure

The inferred microstructural parameters summarized in Table 2 reveal an important peculiarity that the microstructure of snow/firn deposits varies according to the conditions of ice formation. As a first approximation, the examined ice cores can be empirically divided in two groups on the basis of the dense packing characteristics (the critical coordination number Z_0 and the RDF slope C). One group, distinguished as L-group, exhibits relatively low Z_0 of ~ 6.5-7 and C of ~ 40, while the other group (H-group) is characterized by higher Z_0 of ~ 7.5-8 and C of ~ 50-60. Correspondingly (see Table 2), the respective critical densities are relatively low, $\rho_0 \sim 0.704$-0.714, and higher, $\rho_0 \sim 0.736$-0.754. The L- and H-structural types are typical for low- and high-temperature

extremes (see Table 1). However, it should be emphasized that there is no direct correlation with temperature in the intermediate interval from –40 to –24ºC. The extreme cases (e.g., Mizuho and Summit, KM200 and Site A) occur in similar temperature conditions. As illustrated in Fig. 6a, the critical bonding factor does not vary from one group to the other, and both groups cover the same range of scatter ($\zeta_0 \sim 0.55 \pm 0.05$) when plotted against temperature. Only low surface densities of $\rho_s \sim 0.33$-0.42 are met in the L-group, and the dilatancy exponent β for this group tends to increase with temperature from 3.5 to 8 (Fig. 6b). A value of $\beta \sim 4$ appears to be well established for central Antarctic cores of the L-group under low-temperature conditions (circled cluster in Fig. 6b). The H-group exhibits much higher surface densities $\rho_s \sim 0.38$-0.49 and dilatancy exponents $\beta \sim 8$-10. The results of computational tests (dotted curves in Figs. 5a and f) demonstrate the high sensitivity of the density-depth curves to β in the intermediate range of depths, allowing this parameter to be reliably constrained.

To illustrate the maximum divergence in density profiles for different snow/firn structures, the curves simulated for 3 other sets of microstructural parameters Z_0, C, ζ_0 are compared with the graph for Site A (L-group) in Fig. 5d. The curve 1 for the Crete ice core structure demonstrates the maximum deviation from the Site A core within the same L-group, while the Milcent and Mizuho ice core structures (curves 2 and 3) represent extreme cases from the H-group. Although the density profiles and close-off characteristics fall within a range of ±10% of that for the average structure, the profiles from the L- and H-groups do not overlap, revealing a continuous transition between geometrical and physical properties from one structure group to the other. It can clearly be seen that for similar temperatures and accumulation rates, the L-group has distinctly lower densification rates (i.e., a "harder" structure) in comparison with the H-group. This suggests that other factors, such as wind speed [19, 46] and/or insolation [13], may also play important roles in the formation of snow/firn strata and participate in switching between the densification regimes under changing climate.

In accordance with [46], the surface density is primarily correlated with wind speed, and the Antarctic sites (Pionerskaya, Mizuho, KM200, KM140, and KM105) characterized by intermediate surface temperatures (–39 to –24.5 °C) and strong winds (mean wind velocity > 9-10 m s^{-1}) all fall into the H-group. It can thus be speculated that in this case, the initial surface-snow structure will be closer to perfect, resulting in a denser closest packing at the snow-to-firn transition. In contrast, at low wind speed, typical for sites in the L-group at temperatures below –25 °C, surface snow is less dense [46] and looser. In addition, insolation [13] and surface temperature can play a significant role in snow structure formation, facilitating (especially at relatively low accumulation rates) grain bonding and growth at the expense of smaller ice particles, resulting in smaller values for Z_0, C and ρ_0. For example, direct measurements of the specific pore surface in Vostok and KM200 ice cores [7, 9] have confirmed that pores in snow at Vostok are essentially larger (low void surface area) than at KM200. In this context, the dominance of the H-group at high temperature (> –25 °C) can be attributed not only to windiness but also, at least in part, to high accumulation, masking the insolation and/or effects of high temperature gradients [19].

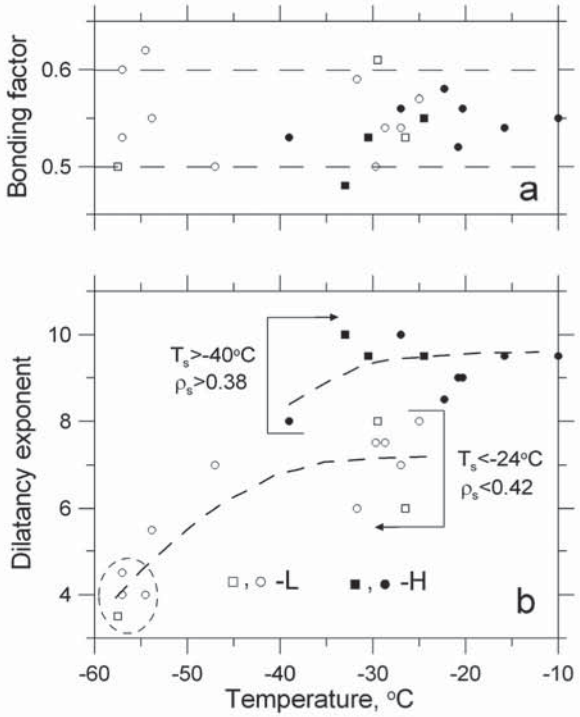

*Figure 6: Critical bonding factor ζ_0 (**a**) and dilatancy exponent β (**b**) for L-group (open symbols) and H-group (solid symbols) plotted against surface temperature. Squares and circles correspond to microstructural parameters constrained by direct stereological measurements and inferred from the density-depth profiles, respectively. Dashed lines show the range of ζ_0 deviations in (**a**) and tendencies of β growth in (**b**).*

As grain restacking in snow can destroy necks and reduce bond areas due to the inevitable shearing of intergranular contact zones, the dynamic equilibrium between grain rearrangement and neck growth due to water-vapor diffusion (ice-mass transport) maintains a certain degree of bonding in excess of dislocation creep without a noticeable direct influence of temperature and snow structure on the critical bonding factor ζ_0 (see Fig. 6a).

In the softer snow structures of the H-group, with a more well-developed specific pore-space surface, the greater intensity of diffusive water-vapor transport interferes with and minimizes the dilatancy effects in the snow densification stage, leading to the highest values of β. The interplay between insolation (surface temperature) and accumulation most likely controls the

growth of the dilatancy index in the L-group, in general correlation with the increase in ice accumulation rates, which reduces the influence of insolation. The BC ice core is an obvious example of a highly dilatant snow structure (i.e., low β) formed at the enhanced contrast between high temperature (insolation) and low accumulation. For comparable accumulation rates but at very low temperatures, the central Antarctic stations of Vostok, Dome Fuji, EPICA DC, Vostok-1, and Komsomolskaya (see Tables 1 and 2) reveal a tendency for β to grow with accumulation rate. The depths corresponding to the critical density (Table 2) also show that, in both groups, ice accumulation significantly interferes in the densification process and perturbs the general tendency of h_0 to decrease with temperature (compare Mizuho and Summit, BC and Site 2, Ushkovsky and Dôme du Goûter cores in Tables 1 and 2).

Table 3: Densification-model parameters and their recommended values.

Parameter	Notation	Value	
		L-group	H-group
Environmental ice-formation conditions			
Relative surface snow density	ρ_s	< 0.42	> 0.38
Surface temperature, ºC	T_s	< -24	> -40
Ice accumulation rate, cm yr^{-1}	b	-	
Microstructural characteristics			
Critical coordination number	Z_0	6.75±0.25	7.75±0.25
RDF slope	C	40	55±5
Critical bonding factor	ζ_0	0.55±0.05	
Dilatancy exponent †	β	3.5-8	8-10
Rheological parameters			
Grain rearrangement-rate constant ‡, MPa^{-1} yr^{-1}	k_r^*	0.022±0.003	
Activation energy of grain rearrangement, kJ mol^{-1}	Q_r	70	
Creep index	α	3.5	
Non-linear viscosity of ice ‡, MPa$^{\alpha}$ yr	μ^*	21±1	
Activation energy of dislocation creep, kJ mol^{-1}	Q_p	58	
Ratio of deviatorically deformed grains	ε	~0.1	
Close-off depth factor	B_h	2.75±0.25	2.42±0.11
Close-off ice-age factor	B_t	2.76±0.24	2.40±0.012

† Correlation with temperature is specified in Fig. 6b
‡ At the reference temperature of $T^* = 215.7$ K

Although the present analysis reveals rather complex relationships between the structure of the snow stratum at the surface of ice sheets and the conditions of ice formation, demonstrating the necessity for further study, the principal tendencies appear to be quite clear. The introduction of two (L- and H-) types of snow build-up with characteristic microstructural parameters essentially reduces the uncertainty of snow/firn densification modeling. The results of constraining the densification model are summarized in Table 3, where the recommended model parameters are given with the corresponding estimated uncertainties. The density profiles simulated using these parameterizations are presented in Figs. 5a-c, Figs. 5e, f, and Appendix D (dashed lines). The deviation of these profiles from the best-fit curves (solid lines) is within ±2-3%, and is comparable to the uncertainty of measurements.

4.2. Characteristic features of snow/firn densification as revealed by modeling

A properly constrained snow/firn densification model makes it possible to discuss the physics of firnification in more detail. Fig. 7 shows the predicted variations of the densification rates and the corresponding components due to ice-particle rearrangement and dislocation creep with respect to depth under different climatic conditions at Vostok and KM200. A temperature increase of up to 30 °C (Table 1) and changes in the snow/firn structure (Table 2) result in a more than ten-fold increase in ω (note the vertical scales in the figure). At low temperatures and relatively small k_r, appreciable plastic deformation ω_p of the porous-ice skeleton develops from the beginning of the snow densification stage (Fig. 7a, dotted curve 2). The fraction x of deviatoric deformation by grain-boundary

sliding in Eq. (4) for the Vostok core thus gradually diminishes with depth from unity to zero (Fig. 7a, dashed curve), as the density and coordination number increase, strengthening the dilatancy effects through parameter λ in Eq. (16). Dilatancy determines the impact of plastic deformation on snow densification, and an increase in λ controlled by β in Eq. (18) (as revealed by Eqs. (16) and (17)) results finally in a rapid drop in ω due to the decrease in ice-grain rearrangement rates ω_r in the middle of the snow stage (Fig. 7a, dotted curve 1).

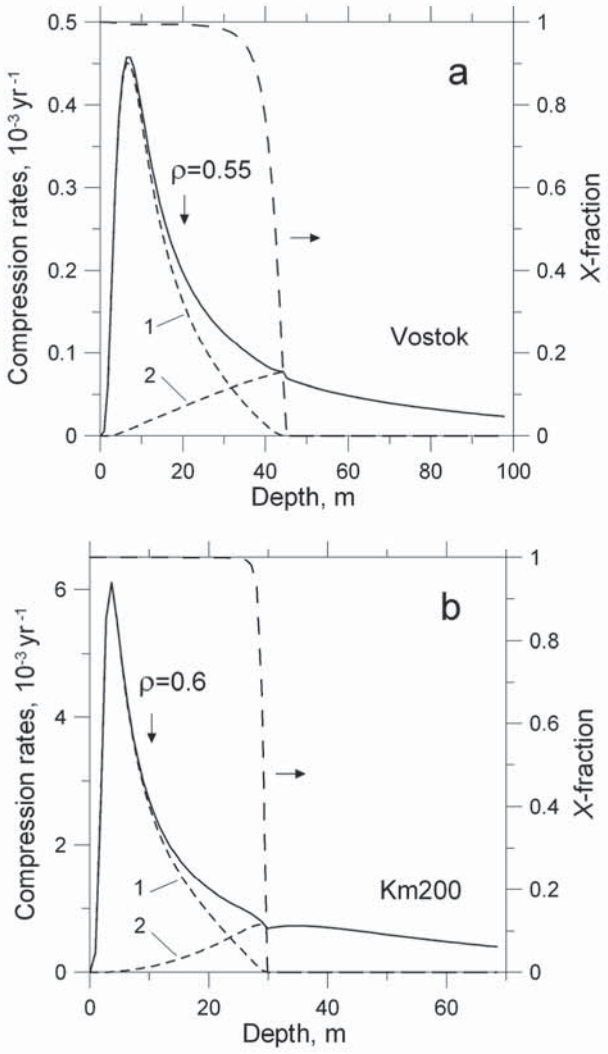

*Figure 7: Total snow/firn compression rates ω (solid lines) and constituent parts ω_r and ω_p due to grain rearrangement and power-law creep (dotted curves 1 and 2, respectively) together with the fraction x of deviatoric strain rates due to grain rearrangement (dashed lines) versus depth at Vostok Station (**a**) and KM200 site (**b**).*

The simulations for KM200 (Fig. 7b) also show that not only the snow/firn densification rates are affected by temperature and snow structure. Due to the non-linear creep of ice ($\alpha > 1$ in Eq. (13)), the growth of k_r at the KM200 site is not counterbalanced by the decrease in μ in Eq. (17). As a result, ice-grain rearrangement practically remains the sole mechanism of deviatoric deformation (i.e., $x \approx 1$) during the entire snow stage (Fig. 7b, dashed curve). However, dilatancy dominates in Eqs. (3) and (4), still controlling ice-crystal rearrangement and plastic deformation in the snow compression (Fig. 7b, dotted curves) described by Eqs. (16) and (17). In the KM200 core, an abrupt decrease in the densification rate occurs at higher densities, where grain-boundary sliding ceases, and the firn stage begins at depth of around 30% shallower than for the Vostok core (see Table 2). In both cases, the critical depth h_0 below which densification occurs solely by the dislocation creep of ice grains can be clearly identified in Fig. 7 as the point at which the fraction of deviatoric deformation by grain rearrangement x becomes zero.

The model predictions indicate that the snow-to-firn transition is characterized by a local perturbation in the compression rates. This peculiarity can be clearly discerned for the low-temperature core from Vostok (Fig. 7a) as a drop in ω caused (due to the interplay between x and λ) by an abrupt increase in the deviatoric stress in Eq. (16) as x falls to zero. At the higher temperatures and relatively low load pressures of the KM200 core, the compression rate in the firn stage starts to grow with depth (with p_l), passing through a local maximum (Fig. 7b). Both effects become more prominent if the deviatoric-stress factor ε in Eq. (16) is increased. Similar changes in the slope of the snow/firn density profiles around relative densities of 0.72-0.78 were observed and explained as due to the emerging dominance of dislocation creep in a series of papers [24, 25, 54]. The critical densities deduced in the present study and given in Table 2 lie within the same range of 0.7-0.76. As shown in Appendix A, ρ_0 is related to the firn structure by the geometrical characteristics Z_0 and C, increasing with these values (Table 2) from the L-group to H-group. The characteristic bend (upper critical point) observed after [6] in the density-depth profiles around relative densities of 0.55-0.6 at approximately half h_0 can be identified here (Fig. 7) with the maximum decrease in snow densification rate due to the dilatancy effects triggering the dislocation creep of ice grains.

In this context, the densification model [8] can be understood as the limiting case of Eqs. (16) and (17) at $\beta \to \infty$ ($\lambda \approx 0$) with k_r renormalized so as to exclude the fraction $1 - x$ of deviatoric deformation by grain plasticity from Eq. (16) for $\rho < \rho_0$ (i.e., $Z < Z_0$) in snow. Such a schematization formally reduces to zero an intermediate interval in which ice-grain restacking and creep work together, making it possible to consider the critical density ρ_0 as independent tuning parameter at appropriately constrained microstructural characteristics Z_0 and C in firn. Inevitably, this simplifies the theoretical representation of density-depth curves. As an example, the density profiles simulated for the 6 basic ice cores (Vostok, Mizuho, Km200, Site A, BC, and KM105) at recommended model parameters from

Table 3 are compared in Fig. 8 (thin solid lines) to those (bold lines) predicted by the model [8] and the corresponding density measurements. Besides the obvious difference in shape, a noticeable mismatch of ±5-7% between the two simulated profiles can be observed, attributable to the ice-core structural variability between the L- and H-groups, which was not taken into account in previous studies.

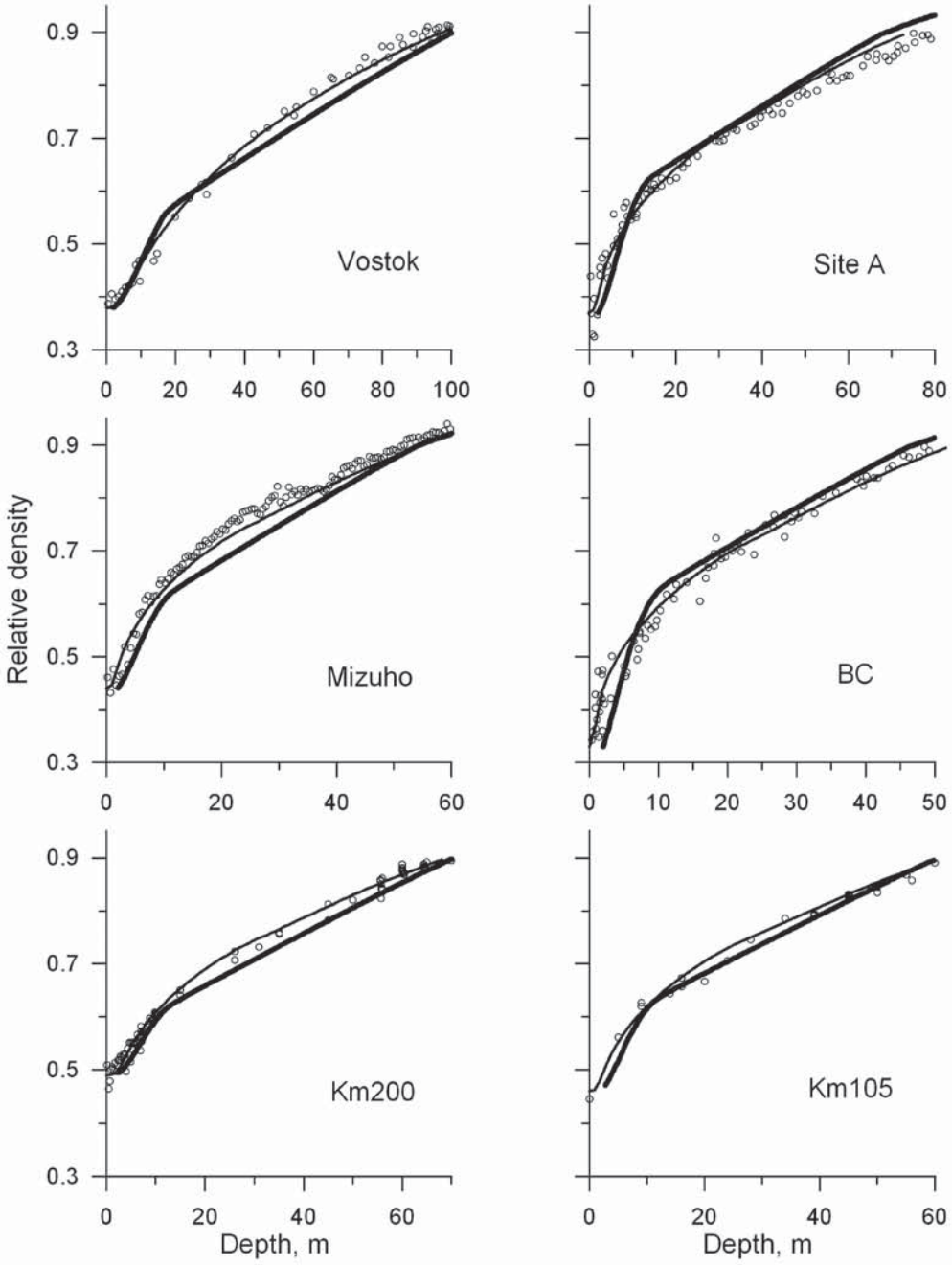

Figure 8: Comparison of density-depth profiles for basic ice cores from Vostok, Mizuho KM200, Site A, BC, and KM105 (thin solid lines) with the predictions of the model [8] (bold lines). Open circles denote experimental data (see Table 1).

It is also interesting to compare the results of the present model with detailed snow density measurements near the ice-sheet surface, where different depositional, diagenetic and meteorological processes (not taken into account in modeling) are superimposed on the modeled pressure sintering and may even dominate in the densification process. As shown in the inset of Fig. 5a, and as expected [3], systematically higher densification rates are observed at Vostok within the uppermost 3-5 m compared to the computations. However, the deeper part of the simulated density profile closely follows the observational data.

4.3. Paleoclimatic implications of the snow/firn densification model

One of the most important applications of a snow/firn densification model is in providing the basis for predicting the difference between the ice age and the age of atmospheric gases occluded in the ice (e.g., [12, 15, 33, 65, 67]). Accurate simulation of the gas age – ice age relationship is a key question of deriving reliable paleoclimatic histories from ice cores. In this context, the depth h_{off} and ice age t_{off} in firn at the close-off density ρ_{off} are the principal characteristics related to trapping atmospheric gases in the snow/firn densification process. As the pore closure problem is not considered explicitly here, a simplified empirical correlation (24) between ρ_{off} and temperature [47, 51, 52] is used in calculations. The best-fit present-day close-off characteristics for all selected ice cores are listed in Table 2. A reliably constrained physical model can be further employed as a robust instrument to study relationships between ρ_{off}, h_{off}, and t_{off} as well as their dependences on climate.

Under quasi-stationary ice-formation conditions, a certain similarity between different density-depth profiles scaled by the typical values of ρ_0 and h_{off} can be envisaged, with the product $\rho_0 h_{off}$ being correlated (approximately equal) to bt_{off}. Direct calculations based on the data from Tables 1 and 2 confirm this expectation and show that the critical density ρ_0 is very close to the mean snow/firn density. The same approach can be applied for scale analysis of Eq. (16), which permits approximate integration with respect to depth from 0 to h_{off} after neglecting deviatoric stresses ($\varepsilon \approx 0$), substituting Eqs. (1) and (20) at $\dot{e}_1 = 0$, and assuming $p_l \approx g\rho_i\rho_0 h$ instead of Eq. (19). This leads to two simplified expressions for t_{off} and h_{off}:

$$t_{off} = B_t \left[\frac{\mu \rho_0^{\alpha}}{(g\rho_i b)^{\alpha}} \right]^{1/(1+\alpha)}, \qquad h_{off} = B_h \left[\frac{\mu b}{(g\rho_i)^{\alpha} \rho_0} \right]^{1/(1+\alpha)} \equiv \frac{B_h b}{B_t \rho_0} t_{off}, \tag{25}$$

where B_t and B_h are the dimensionless form factors of the density-depth profile and ρ_0 is determined by Z_0 and C (see Appendix A). For non-zero values of $\dot{e}_1$, the accumulation rate b in Eqs. (25) should be replaced by the difference $b - 0.5\rho_0 \dot{e}_1 h_{off}$.

The values of B_t and B_h calculated for the deduced close-off characteristics are given in Table 2 and summarized in Table 3. As might be expected, the coefficients B_t and B_h are practically identical and can be regarded as generalized attributes of different types of snow, both ranging from 2.3 to 2.5 for the H-group and from 2.5 to 3.0 for the L-group. As these findings are originally based on the fitting of theoretical profiles to field observations and thus are independent of possible interpretations derived from model parameters, B_t and B_h are considered to reflect the intrinsic peculiarities of the densification phenomenon and its relationship with the snow/firn structure and ice formation conditions. Sensitivity tests show that the variations in B_t and B_h within each group do not exceed ±1.5% and ±3% over a ±50% range of accumulation rate and ±10 °C range of temperature, respectively. Once original mircostructural properties of snow/firn deposits and local quasi-stationary ice-formation conditions have been specified in terms of the B-factors (e.g., based on present-day ice core measurements), Eqs. (25) together with the first of Eqs. (22) become a useful tool for ice core data analyses and can be employed directly for predicting quasi-stationary close-off characteristics under different climates within a certain group.

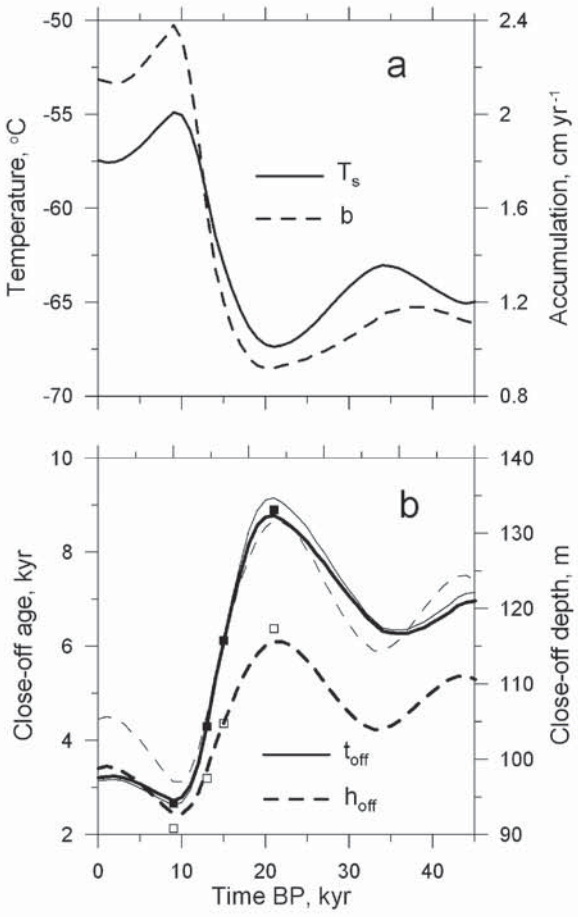

*Figure 9: Paleoclimatic variations of close-off characteristics at Vostok Station for the last 45 kyr. **(a)** Ice-formation conditions (T_s and b) [72] and **(b)** quasi-stationary close-off depth h_{off} and ice age t_{off} calculated from Eqs. (25) (bold lines) and from the model [8] (thin lines), respectively. Open and solid squares denote h_{off} and t_{off} predicted by the proposed general model.*

The central Antarctic sites of deep drilling projects are of special interest. They are characterized by very

similar present-day B-factors, $B_t \approx 2.87 \pm 0.13$ and $B_h \approx 2.89 \pm 0.11$, which in accordance with sensitivity tests are not expected to vary by more than 3% during glacial periods. Recent 45 kyr histories of surface temperatures and accumulation rates (Fig. 9a) reconstructed at Vostok Station [72] have been used to illustrate the possible paleoclimatic implications of the developed densification model and the simplified equations (25). The corresponding variations in h_{off} and t_{off} simulated in the quasi-stationary approximation are shown in Fig. 9b. The bold curves for h_{off} and t_{off} are calculated from Eqs. (25) at the mean values of $B_t = 2.76$ and $B_h = 2.82$ estimated for the assumed climate changes at Vostok, using the best-fit microstructural parameters from Table 2. The respective close-off characteristics predicted by the general model are shown in Fig. 9b for 9, 13, 15, and 21 kyr before present (B.P.) by open and solid squares. As predicted above, the deviation does not exceed 2-3%. The corresponding quasi-stationary density-depth profiles at the climatic extremes of the Holocene optimum (9 kyr B.P.) and the Last Glacial Maximum (21 kyr B.P.) are plotted in Fig. 10.

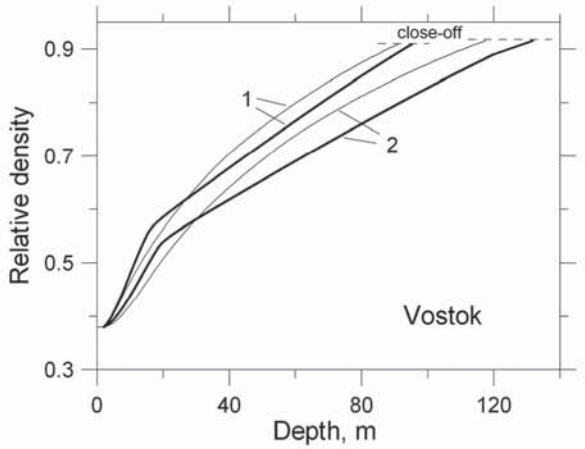

Figure 10: Quasi-stationary density-depth profiles at Vostok for the past temperature extremes at 9 and 21 kyr B.P. (curves 1 and 2, respectively) determined by the present model (thin lines) and by the model [8] (bold lines).

Comparison of these results with the predictions of the model [8] reveals good agreement between the t_{off}-curves, whereas substantially greater depths of pore closure h_{off} are obtained in the framework of the approach [8] during cold periods (see Fig. 9b, thin curves). This mismatch can easily be understood by comparison of the density-depth profiles produced by the different models (see Fig. 10). In case of [8] (Fig. 10, bold curves), ice grain rearrangement in the snow stage ceases at relatively low critical density which is also assumed to decrease with decreasing temperature. Thus, the densification rates become considerably smaller in the intermediate part of the density profile with unreasonably early snow-to-firn transition, particularly at low temperatures. This effect artificially diminishes the mean snow/firn density and as follows from the second of Eqs. (25), increases the close-off depth in comparison with more sophisticated description of snow densification proposed in the present work (Fig. 10, thin curves). It should be noted that independent studies [33, 70] of isotopic separation process of permanent atmospheric gases (^{15}N of molecular nitrogen and ^{40}Ar of argon) in polar firn also support shallower close-off depths than those predicted by the model [8].

5. Conclusion

The densification process of snow/firn deposits at the ice sheet surface is a vertical (uniaxial) compression with non-zero deviatoric stresses and strain rates superimposed on global glacier motion. The overall macroscopic deformation in the granular ice compact is attributable to a combination of the rearrangement of grains as rigid particles, and the plastic deformation of grains. Dilatancy effects are revealed in the kinematic relationship between the macroscopic compression and deviatoric strains in ice-grain restacking. The increasing overburden pressure from the very beginning of the snow densification stage acts through intergranular contact forces, which are resolved into grain-boundary sliding and dislocation creep of ice crystals. The grain rearrangement ceases at the critical snow density (coordination number), and the firn stage sets on controlled solely by plastic deformation of ice grains.

The microscopic geometry of the ice-grain structure is described via Alley's linear correlation [2] between the relative density and the coordination number in snow, and is represented in the framework of Arzt's scheme [10] (see Appendix A) in the firn stage. Grain bonding and neck growth (agglomeration) effects are taken into account in the proposed model by introducing a new structural parameter ζ, the fraction of free grain surface not consumed by plastically formed contacts but occupied by excess neck volume created due to water-vapor transport. In accordance with stereological observations, ζ is assumed to be a linear function of the coordination number. Thus, only the critical coordination number Z_0, the slope C of the cumulative ice-grain radial distribution function, and ζ_0 at the critical point of the snow-to-firn transition control the evolution of the snow/firn structure with increasing density in Eqs. (9)-(11). As shown in Appendix A, the critical density ρ_0 is uniquely determined by Z_0 and C.

The physical model (1), (16)-(23) for snow/firn densification in arbitrary non-stationary climatic conditions is proposed. These equations are based on Alley's description [2] of snow compaction by grain-boundary sliding, taking into account dilatancy effects in ice-grain rearrangement, and use an improved solution for intergrain contact zone deformation by power-law creep (see Appendix B). Gubler's concept [36] of "force chains" conducting external stresses in polydisperse ice-grain structures is employed to construct the phenomenological relations (14), (16) and

(15), (17) for effective pressure and deviatoric stresses on grain contacts. The creep index α and the non-linear viscosity μ in the ice flow law (13) together with the grain-rearrangement rate constant k_r and the dilatancy exponent β introduced in Eqs. (17) and (18) are the principal model parameters responsible for the macroscopic rheological behavior of the snow/firn compact.

The model is constrained and validated on a representative set of ice core data (see Table 1) which covers a wide ranges of present-day temperature (–57.5 to –10 °C) and ice accumulation rate (2.2 to 330 cm yr^{-1}) conditions. The measured snow/firn density profiles and available data on ice core structures allow the rheological parameters to be reliably determined, giving $k_r^* = 0.022 \pm 0.003$ MPa^{-1} yr^{-1} and $\mu^* = 21 \pm 1$ MPa^{α} yr at the reference (Vostok) temperature of $T^* = 215.7$ K with the respective activation energies $Q_r = 70$ kJ mol^{-1} and $Q_p = 58$ kJ mol^{-1} for the creep exponent $\alpha = 3.5$. The critical densities deduced from the calculations (Table 2) fall within the range of 0.7-0.76, and are explained by the onset of power-creep pressure sintering. The characteristic bend observed after Anderson and Benson [6] at the relative density of 0.55-0.6 is concluded to correspond to the maximum decrease in the snow densification rate due to dilatancy effects with an increasing (although not dominant) influence of the dislocation creep of ice grains. The examined ice cores (Table 2) can be empirically divided in two (L- and H-) groups on the basis of the microstructural parameters Z_0, C, reflecting the conditions of ice formation (surface temperature, ice accumulation, wind) given a common critical bonding factor of $\zeta_0 = 0.55 \pm 0.05$. High-speed winds, intense snow drift, scoring, and other precipitation processes most likely result in higher surface densities and elevated critical coordination numbers, facilitating development of the snow stage. The recommended model parameters are summarized in Table 3. Simplified equations (25) are derived for predicting the depth of pore closure h_{off} in firn and the ice age t_{off} at the close-off. The two groups of snow/firn structure are distinguished in these relations by certain ranges of the dimensionless form factors of density-depth profiles (B_t and B_h). Sensitivity tests show that the form factors are stable with respect to changes in temperature and accumulation rate. These results are applied to simulation and discussion of the paleoclimatic evolution of density-depth profiles and close-off characteristics at Vostok Station.

Further investigations are needed in order to better understand the process of the snow/firn densification and structure development. Dilatancy effects and grain bonding were phenomenologically introduced in the present model via the two parameters β and λ. However, the microscopic behavior controlling these effects remains to be clarified.

Acknowledgements

The authors are grateful to J. Kipfstuhl, H. Narita, F. Nishio, T. Shiraiwa, K. Smirnov, and F. Wilhelms for providing the original ice core density data employed in this study. Valuable discussions with R. Alley, A.V. Kosterin, A.G. Egorov and useful comments by T. Blunier, O. Gagliardini, V.N. Golubev, S.A. Sokratov are also gratefully acknowledged.

This collaborative research is a contribution to Project 4 of the Subprogram "Study and Research of the Antarctic", the Federal Target Program "World Ocean" of the Russian Federation. The present work was supported in Russia through Grant No. 05-05-64797 from the Russian Foundation for Basic Research and in Japan through the Japan Society for the Promotion of Science under the FY2004 JSPS Invitation Program for Research in Japan.

References

[1] R.B. Alley, "Texture of polar firn for remote sensing", Ann. Glaciol., **9**, 1987, pp. 1-4.

[2] R.B. Alley, "Firn densification by grain-boundary sliding: a first model", Journal de Physique (Paris), **48**, Colloque C1 (Supplément au nº3), 1987, pp. 249-254.

[3] R.B. Alley, "Concerning the deposition and diagenesis of strata in polar firn", J. Glaciol., **34**(118), 1988, pp. 283-290.

[4] R.B. Alley and C.R. Bentley, "Ice-core analysis on the Siple Coast of West Antarctica", Ann. Glaciol., **11**, 1988, pp. 1-7.

[5] R.B. Alley and B.R. Koci, "Ice-core analysis at Site A, Greenland: preliminary results", Ann. Glaciol., **10**, 1988, pp. 1-4.

[6] D.L. Anderson and C.S. Benson, "The densification and diagenesis of snow", Ice and Snow. Properties, Processes and Applications, W.D.Kingery (Ed.), M.I.T. Press, Boston, 1963, pp. 391-411.

[7] L. Arnaud, Modelisation de la transformation de la neige en glace a la surface des calottes polaires (Thèse de Doctorat, de l' Université Joseph Fourier de Grenoble), 1997.

[8] L. Arnaud, J.M. Barnola and P. Duval, "Physical modeling of the densification of snow/firn and ice in the upper part of polar ice sheets", Physics of Ice Core Records, T. Hondoh (Ed.), Hokkaido University Press, Sapporo, 2000, pp. 285-305.

[9] L. Arnaud, V. Lipenkov, J.M. Barnola, M. Gay and P. Duval, "Modelling of the densification of polar firn: characterization of the snow-firn transition", Ann. Glaciol., **26**, 1998, pp. 39-44.

[10] E. Arzt, "The influence of an increasing particle coordination on the densification of spherical powders", Acta Metall., **30**, 1982, pp. 1883-1890.

[11] E. Arzt, M.F. Ashby and K.E. Easterling, "Practical applications of hot-isostatic pressing diagrams: four case studies", Metall. Trans, Ser. A, **14**(2), 1983, pp. 211-221.

[12] J.M. Barnola, P. Pimienta, D. Raynuad and E.S. Korotkevich, "CO_2-climate relationship as deduced from the Vostok ice core: a re-examination based on new measurements and on a re-evaluation of the air dating", Tellus, Ser. B, **43**, 1991, pp. 83-90.

[13] M.L. Bender, "Orbital tuning chronology for the Vostok climate record supported by trapped gas composition", Earth Planet. Sci. Lett., **204**, 2002, pp. 275-289.

[14] C.S. Benson, "Stratigraphic studies in the snow and firn of the Greenland ice sheet", SIPRE Res. Rep., **70**, 1962, pp. 76-83.

[15] T. Blunier, J. Schwander, J. Chappellaz, F. Parrenin and J.M. Barnola, "What was the surface temperature in central Antarctica during the last glacial maximum?" Earth Planet. Sci. Lett., **218**, 2004, pp. 379-388.

[16] R.L. Brown, "A volumetric constitutive law for snow based on a neck growth model", J. Appl. Phys., **51**(1), 1980, pp. 161-165.

[17] R.L. Brown and M.Q. Edens, "On the relationship between neck length and bond radius during compression of snow", J. Glaciol., **37**(126), 1991, pp. 203-208.

[18] M. Budhu, Soil mechanics and foundations, John Wiley & Sons, Inc. New York etc., 2000.

[19] M. Craven and I. Allison, "Firnification and the effects of wind-packing on Antarctic snow", Ann. Glaciol., **27**, 1998, pp. 239-245.

[20] K.M. Cuffey, "Interannual variability of elevation on the Greenland ice sheet: effects of firn densification, and establishment of a multi-century benchmark", J. Glaciol., **47**(158), 2001, pp. 369-377.

[21] Dome-F Ice Core Research Group, "Preliminary investigation of paleoclimate signals recorded in the ice core from Dome Fuji station, East Dronning Maud Land, Antarctica", Ann. Glaciol., **27,** 1998, pp. 338-342.

[22] P. Duval, M.F. Ashby and I. Anderman, "Rate-controlling processes in the creep of polycrystalline ice", J. Phys. Chem., **87**, 1983, pp. 4066-4074.

[23] T. Ebinuma and N. Maeno, "Experimental studies on densification and pressure-sintering of ice", Ann. Glaciol., **6**, 1985, pp. 83-86.

[24] T. Ebinuma and N. Maeno, "Particle rearrangement and dislocation creep in snow-densification process", Journal de Physique (Paris), **48**, Colloque C1 (Supplément au°3), 1987, pp. 263-269.

[25] T. Ebinuma, H. Nishimura and N. Maeno, "A new explanation of bending of snow density profile", Memoirs of National Institute of Polar Research, Special Issue 39, 1985, pp. 184-188.

[26] M.Q. Edens and R.L. Brown, "Changes in microstructure of snow under large deformations", J. Glaciol., **37**(126), 1991, pp. 193-202.

[27] A.A. Ekaykin, V.Ya. Lipenkov, J.R. Petit and V. Masson-Delmotte, "50-ti letnii tsikl v izmeneniyah akkumulyatsii i izotopnogo sostava snega na stantsii Vostok [50-year cycle in variations of accumulation rate and isotopic composition of snow at Vostok Station]", Mater. Glyatsiol. Issled. [Data of Glaciological Studies], **94**, 2003, pp. 163-173.

[28] EPICA community members, "Eight glacial cycles from an Antarctic ice core", Nature, **429**, 2004, pp. 623-628.

[29] H.F. Fischmeister and E. Arzt, "Densification of powders by particle deformation", Powder Metall., **26**(2), 1983, pp. 82-88.

[30] O. Gagliardini and J. Meyssonnier, "Flow simulations of a firn-covered cold glacier", Ann. Glaciol., **24**, 1997, pp. 242-248.

[31] S. Gerlan, H. Oerter, J. Kipfstuhl, F. Wilhelms, H. Miller and W.D. Miners, "Density log of a 181 m long ice core from Berkner Island, Antarctica", Ann. Glaciol., **29**, 1999, pp. 215-219.

[32] V.N. Golubev and S.A. Sokratov, "Regular packing of grains as a model of snow structure", Ann. Glaciol., **38**, 2004, pp. 25-29.

[33] C. Goujon, J.M. Barnola and C. Ritz, "Modeling the densification of polar firn including heat diffusion: Application to close-off characteristics and gas isotopic fractionation for Antarctica and Greenland sites", J. Geophys. Res., **108**(D24), 2003, pp. 4792-4809.

[34] A.J. Gow, "Deep core studies of the accumulation and densification of snow at Byrd Station and Little America V, Antarctica", CRREL Res. Rep. 197, 1968.

[35] A.J. Gow, "Time-temperature dependence of sintering in perennial isothermal snowpacks", Snow Mechanics, IAHS Publ. No. 114, 1975, pp. 25-41.

[36] H. Gubler, "Determination of the mean number of bonds per snow grain and of the dependence of the tensile strength of snow on stereological parameters", J. Glaciol., **20**(83), 1978, pp. 329-341.

[37] E.V. Guseva and V.N. Golubev, "Matematiches-kaya model formirovaniya stroeniya i svoystv snezhnogo pokrova [Mathematical model of snow cover structure and properties formation]", Mater.

Glyatsiol. Issled. [Data of Glaciological Studies], **68**, 1990, pp. 18-25.

[38] A.C. Hansen and R.L. Brown, "An internal state variable approach to constitutive theories for granular materials with snow as an example", Mech. Mater., **7**(2), 1988, pp. 109-119.

[39] M.M. Herron and C.C. Langway, Jr., "Firn densification: an empirical model", J. Glaciol., **25**(93), 1980, pp. 373-385.

[40] T. Hondoh, H. Shoji, O. Watanabe, E.A. Tsyganova, A.N. Salamatin and V.Ya. Lipenkov, "Average time scale for Dome Fuji ice core, East Antarctica", Polar Meteorol. Glaciol., **18**, 2004, pp. 1-18.

[41] J.B. Johnson and M.A. Hopkins, "Identifying microstructural deformation mechanisms in snow using discrete-element modeling", J. Glaciol., **51**(174), 2005, pp. 432-442.

[42] T. Kameda, N. Azuma, T. Furukawa, Y. Ageta and S. Takahashi, "Surface mass balance, sublimation and snow temperatures at Dome Fuji Station, Antarctica, in 1995", Proc. NIPR Symp. Polar Meteorol. Glaciol., **11**, 1997, pp. 24-34.

[43] T. Kameda, H. Shoji, K. Kawada, O. Watanabe and H.B. Clausen, "An empirical relation between overburden pressure and firn density", Ann. Glaciol., **20**, 1994, pp. 87-94.

[44] C.C. Langway, Jr., "Stratigraphic analysis of a deep ice core from Greenland", CRREL Res. Rep. 77, 1967.

[45] V.Ya. Lipenkov, "Air bubbles and air-hydrate crystals in the Vostok ice core", Physics of Ice Core Records, T. Hondoh (Ed.), Hokkaido University Press, Sapporo, 2000, pp. 327-358.

[46] V.Ya. Lipenkov, A.A. Ekaykin, N.I. Barkov and M. Purshe, "O svyazi plotnosti poverhnostnogo sloya snega v Antarktide so skorostyu vetra [On connection of density of surface ice layer in Antarctica with wind velocity]", Mater. Glyatsiol. Issled. [Data of Glaciological Studies], **85**, 1998, pp. 148-158.

[47] V.Ya. Lipenkov, O.A. Ryskin and N.I. Barkov, "O svyazi mezhdu kolichestvom vozdushnyh vklyucheniy vo l'du i usloviyami l'doobrazovaniya [Relationship of number of air inclusions in ice with ice formation conditions]", Mater. Glyatsiol. Issled. [Data of Glaciological Studies], **86**, 1999, pp. 75-91.

[48] V.Ya. Lipenkov, A.N. Salamatin and P. Duval, "Bubbly-ice densification: II Applications", J. Glaciol., **43**(145), 1997, pp. 397-407.

[49] N. Maeno and T. Ebinuma, "Pressure sintering of ice and its implication to the densification of snow at polar glaciers and ice sheets", J. Phys. Chem., **87**(21), 1983, pp. 4103-4110.

[50] P. Mahajan and R.L. Brown, "A microstructure-based constitutive law for snow", Ann. Glaciol., **18**, 1993, pp. 287-294.

[51] P. Martinerie, V.Ya. Lipenkov, D. Raynaud, J. Chappellaz, N.I. Barkov and C. Lorius, "Air content paleo record in the Vostok ice core (Antarctica): a mixed record of climatic and glaciological parameters", J. Geophys. Res., **99**(D5), 1994, pp. 10,565-10,576.

[52] P. Martinerie, D. Raynaud, D.M. Etheridge, J.M. Barnola and D. Mazaudier, "Physical and climatic parameters which influence the air content in polar ice", Earth Planet. Sci. Lett., **112**(1-4), 1992, pp. 1-13.

[53] K.J. Miller, The physical properties and fabrics of two 400 m deep ice cores from interior Greenland (MA thesis, State Univ. of N.Y., Buffalo), 1978.

[54] H. Narita, N. Maeno and M. Nakawo, "Structural characteristics of firn and ice cores drilled at Mizuho Station, East Antarctica", Memoirs of National Institute of Polar Research, Special Issue 10, 1978, pp. 48-61.

[55] V.N. Nikolaevskii and N.M. Syrnikov, "O ploskom predel'nom techenii sypuchey dilatiruyuschey sredy [On a planar limiting flow of dry dilating medium]", Izvestiya Akad. Nauk U.S.S.R. "Mekhanika tvyordogo tela", No. 2, 1970, pp. 159-166.

[56] V.N. Nikolaevskii, N.M. Syrnikov and G.M. Shefter, "Dinamika uprugo-plasticheskih dilatiruyuschih sred [Dynamics of elastic-plastic dilating media]", Uspehi mehaniki deformiruemyh sred, Nauka, Moscow, 1975, pp. 397-413.

[57] F. Nishio and 13 others, "Annual-layer determinations and 167 year records of past climate of H72 ice core in east Dronning Maud Land, Antarctica", Ann. Glaciol., **35**, 2002, pp. 471-479.

[58] N.I. Osokin, R.S. Samoylov and A.V. Sosnovskiy, "Otsenka teplomassoobmena v pripoverhnostnom sloe snega s uchyotom pronikayuschey radiatsii [Assessment of heat and mass transfer in near-surface snow stratum with regard to penetrating radiation]", Mater. Glyatsiol. Issled. [Data of Glaciological Studies], **96**, 2004, pp. 127-132.

[59] C. Ritz, L. Lliboutry and C. Rado, "Analysis of a 870 m deep temperature profile at Dome C", Ann. Glaciol., **3**, 1982, pp. 284-289.

[60] A.N. Salamatin, V.Ya. Lipenkov, J.M. Barnola, A. Hori, P. Duval and T. Hondoh, "Basic approaches to dry snow-firn densification modeling", Mater. Glyatsiol. Issled. [Data of Glaciological Studies], **101**, 2006, pp. 3-16.

[61] A.N. Salamatin, V.Ya. Lipenkov and P. Duval, "Bubbly-ice densification in ice sheets: I. Theory", J. Glaciol., **43**(145), 1997, pp. 387-396.

[62] A.N. Salamatin, E.A. Tsyganova, V.Ya. Lipenkov and J.R. Petit, "Vostok (Antarctica) ice-core time scale from datings of different origins", Ann. Glaciol., **39**, 2004, pp. 283-292.

[63] C. Scapozza and P. Bartelt, "Triaxial tests on snow at low strain rate. Part II. Constitutive behaviour", J. Glaciol., **49**(164), 2003, pp. 91-101.

[64] M. Schneebeli and S.A. Sokratov, "Tomography of temperature gradient metamorphism of snow and associated changes in heat conductivity", Hydrol. Process., **18**, 2004, pp. 3655-3665.

[65] J. Schwander, "The transformation of snow to ice and the occlusion of gases", The Environmental Record in Glaciers and Ice Sheets, H. Oeschger, and C.C. Langway, Jr. (Eds.), John Wiley and Sons, New York, 1989, pp. 53-67.

[66] J. Schwander, J.M Barnola, C. Andrie, M. Leuenberger, A. Ludin, D. Raynaud and B. Stauffer, "The age of the air in the firn and the ice at Summit, Greenland", J Geophys. Res., **98**(D2), 1993, pp. 2831-2838.

[67] J. Schwander, T. Sowers, J.M. Barnola, T. Blunier, A. Fuchs and B. Malaizé, "Age scale of the air in the summit ice: Implication for glacial-interglacial temperature change", J. Geophys. Res., **102**(D16), 1997, pp. 19,483-19,493.

[68] T. Shiraiwa and 8 others, "Characteristics of a crater glacier at Ushkovsky volcano, Kamchatka, Russia, as revealed by the physical properties of ice cores and borehole thermometry", J. Glaciol., **47**(158), 2001, pp. 423-432.

[69] K.E. Smirnov, "Issledovaniya razreza lednikovogo pokrova v royone stantsii Pionerskaya (Vostochnaya Antarktida) [Studies of the cross-section of the ice sheet in the vicinities of Piorenerskaya Station (East Antarctica)]", Mater. Glyatsiol. Issled. [Data of Glaciological Studies], **46**, 1983, pp. 128-132.

[70] T. Sowers, M. Bender, D. Raynaud and Y.S. Korotkevich, "The $\delta^{15}N$ of N_2 in air trapped in polar ice: A tracer of gas transport in the firn and a possible constraint on ice age – gas age differences", J. Geophys. Res., **97**(D14), 1992, pp. 15,683-15,697.

[71] M.K. Spencer, R.B. Alley and T.T. Greyts, "Preliminary firn-densification model with 38-site dataset", J. Glaciol., **47**(159), 2001, pp. 671-676.

[72] E.A. Tsyganova and A.N. Salamatin, "Non-stationary temperature field simulation along the ice flow line "Ridge B – Vostok Station", East Antarctica", Mater. Glyatsiol. Issled. [Data of Glaciological Studies], **97**, 2004, pp. 57-70.

[73] K.F. Voytkovskiy, Mekhanicheskiye svoystva snega [Mechanical properties of snow], Nauka, Moscow, 1977.

[74] O. Watanabe, K. Kato, K. Satow and F. Okuhira, "Stratigraphic analyses of firn and ice at Mizuho Station", Memoirs of National Institute of Polar Research, Special Issue 10, 1978, pp. 25-47.

[75] O. Watanabe and 12 others, "Preliminary discussion of physical properties of the Dome Fiji shallow ice core in 1993, Antarctica", Proc. NIPR Symp. Polar Meteorol. Glaciol., **11**, 1997, pp. 1-8.

[76] D.S. Wilkinson and M.F. Ashby "Pressure sintering by power law creep", Acta Metall., **23**, 1975, pp. 1277-1285.

Appendix A. Firn-structure characteristics

In accordance with Arzt's approach [10], as schematically illustrated in Fig. 2, the ice-grain structure development is described as concentric expansion ('growth') of centre-fixed spherical particles. The current 'fictitious' equivalent-sphere radius R' normalized by the initial radius R. is defined as

$$R' = (\rho/\rho_0)^{1/3} . \qquad \text{(A1)}$$

Summing after [10] the excess volumes of spherical caps "cut" from the reference spherical grain of radius R' and distributed evenly across its free surface, as shown in Fig. 2, we arrive at the transcendental ice-volume conservation equation relating the radius R'' of the obtained truncated sphere to R'.

$$R'^3 = R''^3 - \frac{Z_0}{4}(R''-1)^2(2R''+1) - \frac{C}{16}(R''-1)^3(3R''+1) \cdot \qquad \text{(A2)}$$

Correspondingly, the fraction of the free surface of the truncated sphere of radius R'' is

$$s = 1 - \frac{Z_0}{2}\frac{R''-1}{R''} - \frac{C}{4}\frac{(R''-1)^2}{R''} . \qquad \text{(A3)}$$

An average cylindrical neck formed at the plastic contact on the reference grain "consumes" the truncated spherical surface, the area of which is $4\pi R'^2(1-(1-\zeta)s)/Z$, yielding directly the relative bond area in units of R^2

$$a = \frac{4\pi R''^2\left[1-(1-\zeta)s\right]}{R'^2 Z}\left[1 - \frac{1-(1-\zeta)s}{Z}\right] .$$

The fraction of grain surface area involved in the grain bonds is thus

$$s_b = aZ/(4\pi) .$$

It is important to note that in snow, at $s = R' = R'' = 1$, the mean bond area remains constant if $\zeta/Z = \zeta_0/Z_0$ and

$$a = a_0 = \frac{4\pi\zeta_0}{Z_0}\left[1 - \frac{\zeta_0}{Z_0}\right] .$$

Accordingly, the total spherical surface (of radius R'') per contact is $4\pi R''^2/Z$. The equivalent spherical cup has the relative base area

$$A = \frac{4\pi R''^2}{R'^2 Z}\left(1 - \frac{1}{Z}\right) .$$

The segment cut from this cap by the bond plane (see Fig. 2) is regarded as the ice grain contact zone in which plastic deformation predominantly takes place.

In the framework of Arzt's scheme [10], the process of densification stops at full density $\rho = 1$ when the grain packing is converted into a space-filling stack of polyhedrons. This limit is reached at $s = 0$ with the corresponding maximum value of $R'' = R''_{max}$, which can be easily calculated from Eq. (A3) as

$$R''_{\max} = 1 + \frac{\left[(Z_0 - 2)^2 + 4C\right]^{1/2} - Z_0 + 2}{C} .$$

The corresponding maximum value of $R' = R'_{max}$ obtained from Eq. (A2) determines the critical density in Eq. (A1) at $\rho = 1$, i.e.,

$$\rho_0 = (1/R'_{max})^3 .$$

Appendix B. Power-law creep of contact zones

Ice powder compaction by grain creep in accordance with [10] is modeled as grain growth (see Fig. 2). From definitions (1), (2) and (A1),

$$\omega_p = \frac{1}{R'}\frac{dR'}{dt} .$$

The contact faces in this scheme are fixed, and the flow rate of ice volume squeezed from under a single contact area a' is

$$V' = \frac{4\pi R'^2}{Z}\frac{dR'}{dt}\left[1 - (1 - \zeta)s\right] .$$

As shown in Fig. 2, it is assumed that this process is approximately a uniaxial compression of the contact segments with the flat base A' parallel to the bond plane. Each segment contains one neck and occupies a portion of the free grain surface $4\pi R''^2 s/Z$ relative to one contact, where the height of the segment is given by

$$H' = 2R''s/Z .$$

Consequently, the axial strain rate averaged over the segment thickness can be expressed via ω_p as

$$\langle \dot{e}_1 \rangle = \frac{V'}{a'H'} = \frac{2\pi R'}{asR''}\left[1 - (1 - \zeta)s\right]\omega_p . \qquad \text{(B1)}$$

An infinitesimal segment layer of radius $r'(h')$ at distance h' from the contact face deforms with strain rate $\dot{e}_1$ under the mean deviatoric axial stress

$$\tau_1 = \frac{2a'}{3\pi r'^2} p_{eff} .$$

The power-creep law (13) then gives

$$\sqrt{3}\mu\dot{e}_1 = \left(\frac{a' p_{eff}}{\sqrt{3}\pi r'^2}\right)^{\alpha} .$$

Integration of this equation over the segment thickness with respect to h' from 0 to H' yields

$$\sqrt{3}\mu\langle \dot{e}_1 \rangle = \frac{1}{H'}\left(\frac{a' p_{eff}}{\sqrt{3}\pi}\right)^{\alpha}\int_0^{H'}\frac{dh'}{r'^{2\alpha}} \approx \left(\frac{a' p_{eff}}{\sqrt{3}a'A'}\right)^{\alpha} . \qquad \text{(B2)}$$

Finally, combining Eqs. (B1) and (B2), the relationship between p_{eff} and ω_p is obtained as

$$p_{eff} = \sqrt{\frac{3A}{a}}\left[\frac{2\sqrt{3}\pi\mu R'}{asR''}\left(1 - (1 - \zeta)s\right)\omega_p\right]^{1/\alpha} .$$

This equation is used to derive Eq. (14).

Appendix C. Mass-conservation law for snow/firn strata

For a given constant density of pure ice ρ_i, the general ice-mass conservation law for the snow/firn stratum of an ice sheet takes the form:

$$\frac{\partial\rho}{\partial t} + \frac{\partial(\rho u)}{\partial x} + \frac{\partial(\rho v)}{\partial y} + \frac{\partial(\rho w)}{\partial h} = 0 ,$$

where x and y are Cartesian coordinates in the horizontal (surface) plane, and u and v are the respective velocities of global ice-sheet motion.

The relative snow/firn density ρ is assumed not to vary in the lateral (horizontal) directions, and u and v are regarded as independent of depth h in a relatively thin surface layer subject to densification. Consequently, multiplication of the mass conservation equation by $g\rho_i$ and substitution of Eq. (19) after the integration with respect to depth from 0 to a certain depth level h yield

$$\frac{\partial p_I}{\partial t} + p_I\left(\frac{\partial u}{\partial x} + \frac{\partial v}{\partial y}\right) + g\rho_i(\rho w - b) = 0 \cdot$$

$$\dot{e}_1 = \frac{\partial u}{\partial x} + \frac{\partial v}{\partial y},$$

Noting that, by definition,

Eq. (20) is arrived at directly.

Appendix D. Comparison of simulated and measured ice-core density profiles

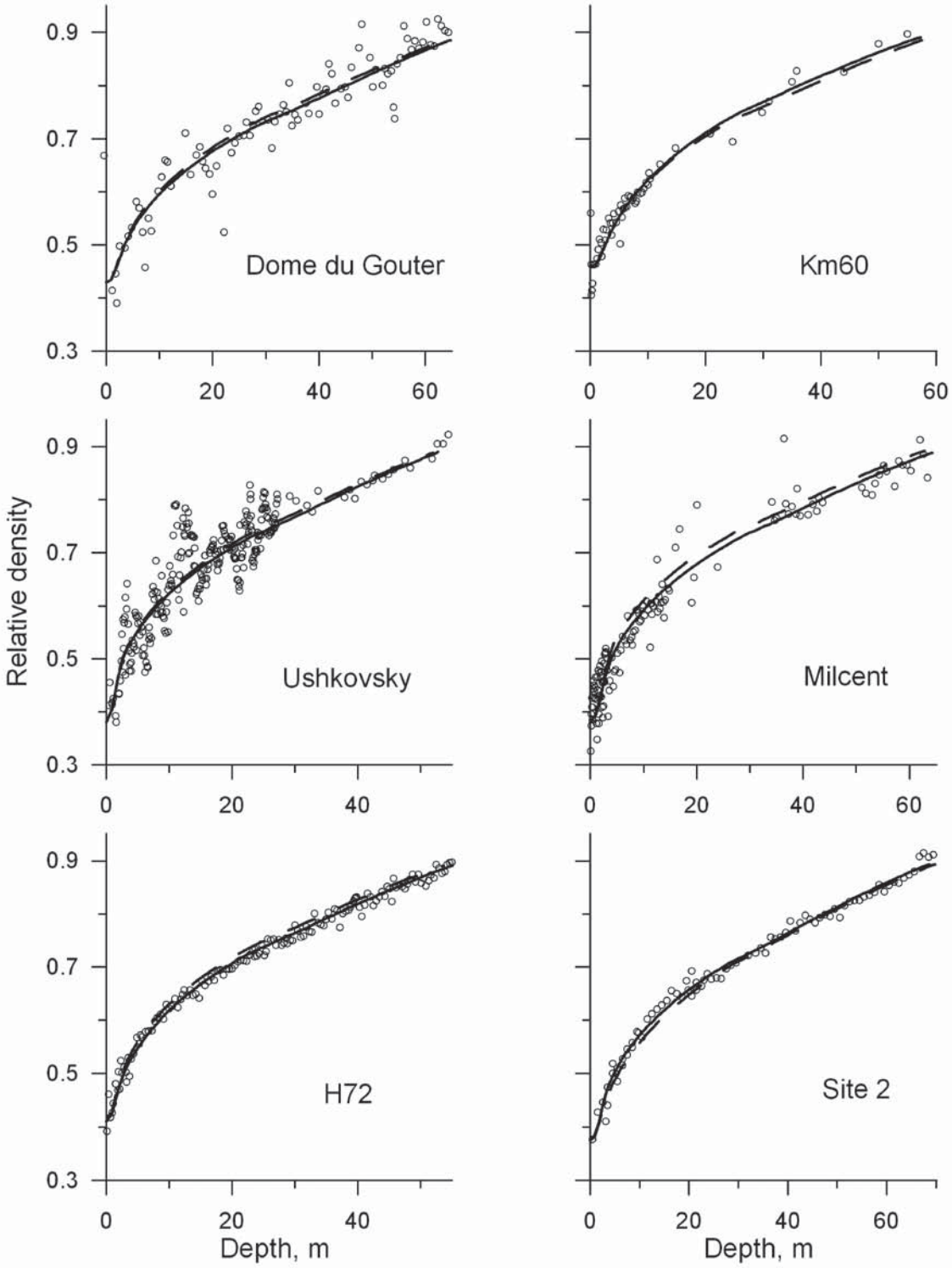

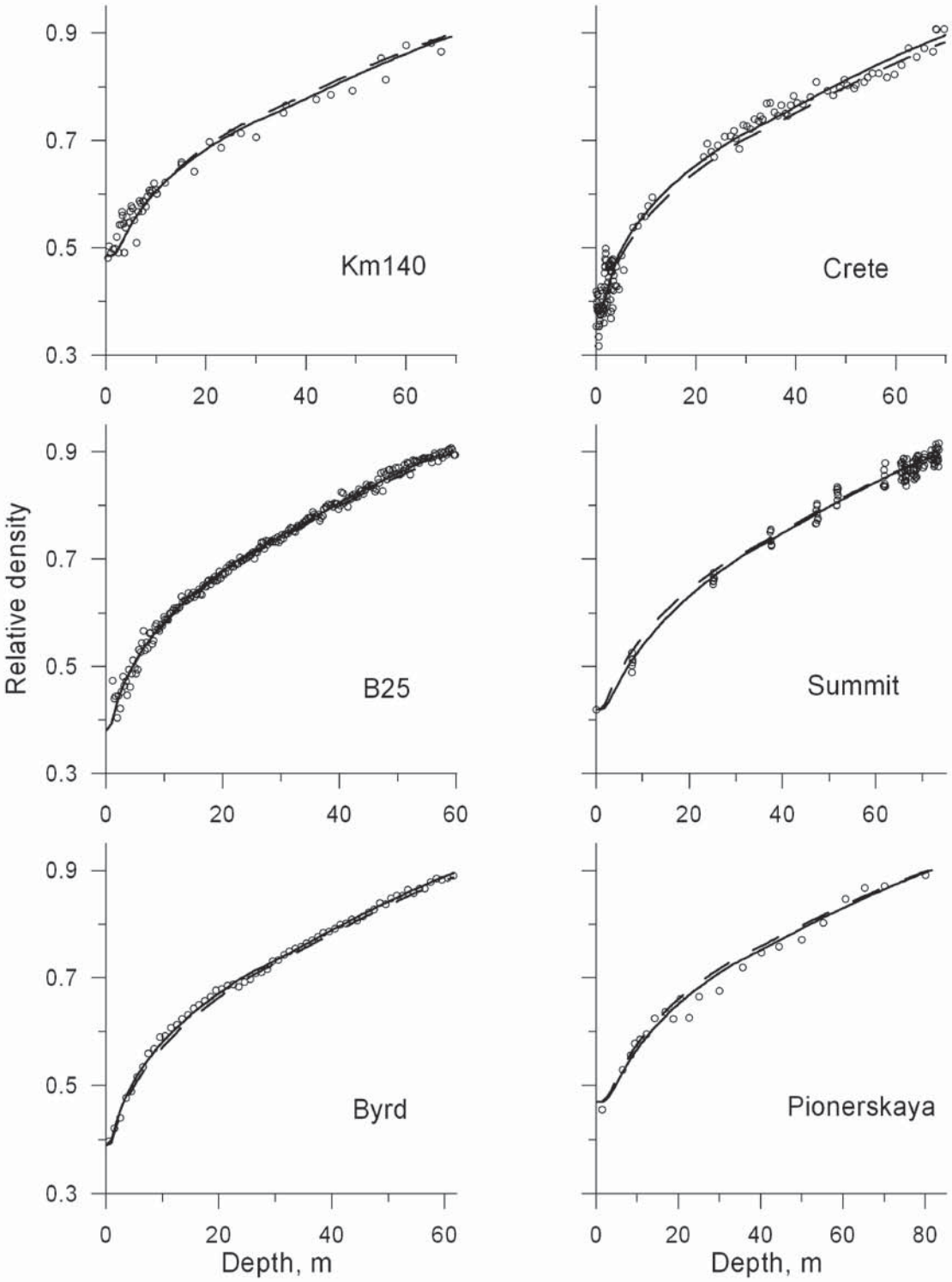
Relative density
Depth, m
Depth, m
Km140
Crete
B25
Summit
Byrd
Pionerskaya
0.9
0.7
0.5
0.3
0
20
40
60
80

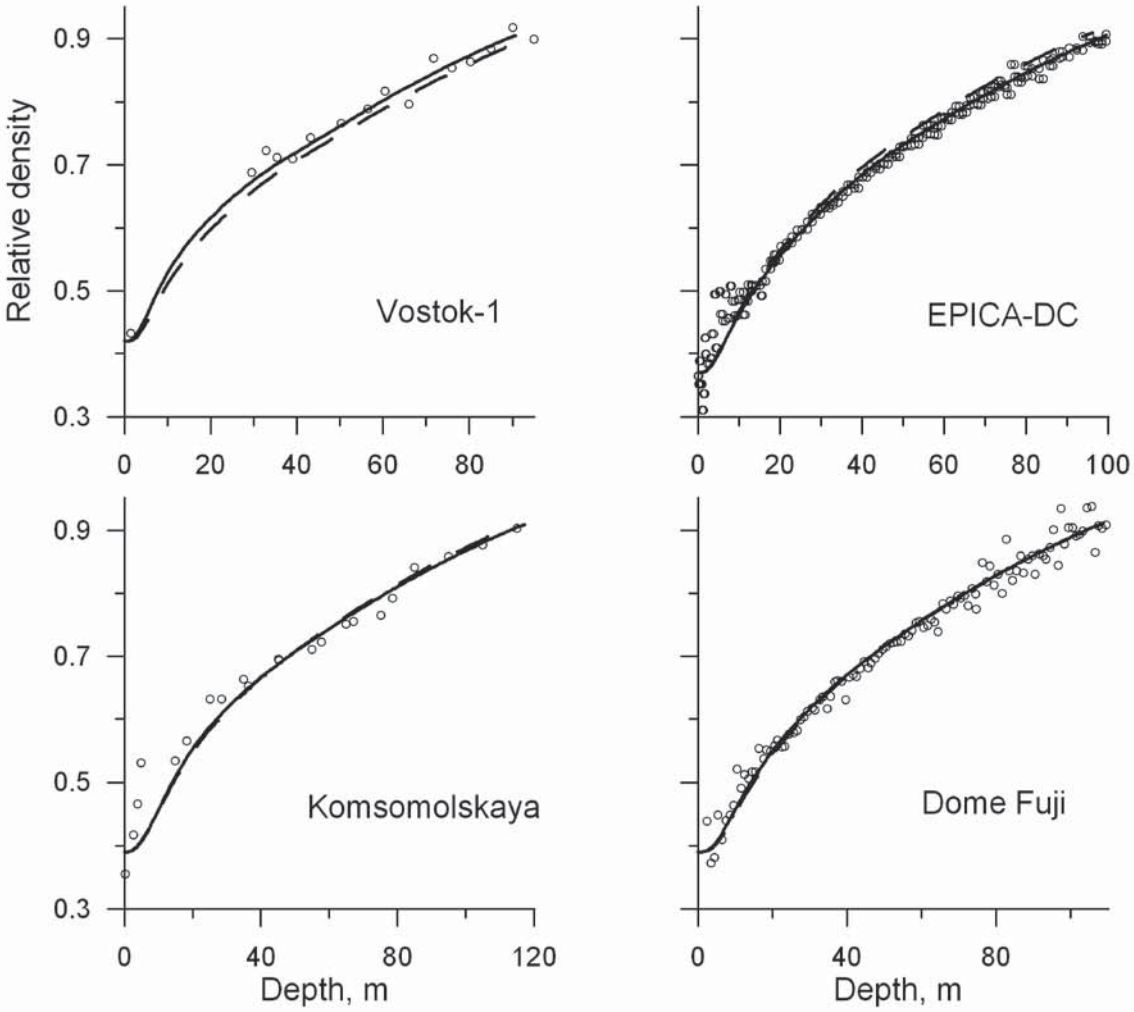
Relative density
0.9
0.7
0.5
0.3
0
20
40
60
80
Vostok-1
EPICA-DC
100
Komsomolskaya
120
Depth, m
Dome Fuji